Hyperonic Stars and the Nuclear Symmetry Energy

Constança Providência[1]*, Morgane Fortin[2], Helena Pais[1] and Aziz Rabhi[3]

[1] Department of Physics, CFisUC-Centro de Física da Universidade de Coimbra, University of Coimbra, Coimbra, Portugal,
[2] N. Copernicus Astronomical Center, Polish Academy of Sciences, Warszawa, Poland, [3] Preparatory Institute for Scientific and Technical Studies, University of Carthage, Tunis, Tunisia

In the present study we analyse the effect of the density dependence of the symmetry energy on the hyperonic content of neutron stars within a relativistic mean field description of stellar matter. For the Λ-hyperon, we consider parametrizations calibrated to Λ-hypernuclei. For the Σ and Ξ-hyperons uncertainties that reflect the present lack of experimental information on Σ and Ξ-hypernuclei are taken into account. We perform our study considering nuclear equations of state that predict two solar mass stars, and satisfy other well-settled nuclear matter properties. The effect of the presence of hyperons on the radius, the direct Urca processes, and the cooling of accreting neutron stars are discussed. Some star properties are affected in a similar way if a soft symmetry energy is considered or hyperonic degrees of freedom are included. To disentangle these two effects it is essential to have a good knowledge of the equation of state at supra-saturation densities. The density dependence of the symmetry energy affects the order of appearance of the different hyperons, which may have direct implications on the neutron star cooling as different hyperonic neutrino processes may operate at the center of massive stars. Models that allow for the direct Urca process, whether they are purely nucleonic or hyperonic ones built consistently with modern experimental data, are shown to have a similar luminosity. It is shown that for a density dependent hadronic model constrained by experimental, theoretical, and observational data, the low-luminosity of SAX J1808.4 − 3658 can only be modeled for a hyperonic NS, suggesting that hyperons could be present in its core.

Keywords: neutron stars, hyperonic stars, symmetry energy, hyperon interaction, neutron star cooling, relativistic mean-field equation of state

1. INTRODUCTION

The behavior of asymmetric nuclear matter is strongly influenced by the density dependence of the symmetry energy of nuclear matter, see (Li et al., 2014) for a review. This quantity defines the properties of systems like nuclei far from the stability line or neutron stars (NS), from the neutron skin thickness to the NS radius (Horowitz and Piekarewicz, 2001a). The advancement of nuclear physics and astrophysics requires, therefore, a well-grounded knowledge of the properties of isospin-rich nuclear matter (Baran et al., 2005; Steiner et al., 2005; Li et al., 2008). In the present study, we will concentrate our attention on the effect of the density dependence of the symmetry energy on some of the properties of hyperonic stellar matter that may occur inside NSs, including the mass and radius of hyperonic stars (Cavagnoli et al., 2011; Vidana et al., 2011; Providência and Rabhi, 2013) or their cooling evolution (Prakash et al., 1992; Yakovlev et al., 2004).

Although the symmetry energy is quite well-constrained at nuclear saturation density, see (Tsang et al., 2012; Lattimer and Lim, 2013; Oertel et al., 2017), its density dependence at high densities is still badly known. The density dependence of the symmetry energy has been investigated in many works, see for instance (Klimkiewicz et al., 2007; Centelles et al., 2009; Tsang et al., 2009; Vidana et al., 2009; Warda et al., 2009; Carbone et al., 2010; Ducoin et al., 2011; Fattoyev et al., 2014), but usually for the saturation and sub-saturation densities. Since the description of NSs requires the knowledge of the equation of state (EoS), from very low to very high densities, it is important to have a correct description of the EoS in the whole range of densities.

Hyperons may have non-zero isospin, and, therefore, their chemical potential depend on the density dependence of the symmetry energy. As a consequence, the fraction of the different hyperonic species reflects the symmetry energy behavior, and, in particular, it has been shown in Providencia and Rabhi (2013) that the onset of the Σ^- and Λ hyperons is sensitive to the slope of the symmetry energy. In the present study we will analyse the interplay between the symmetry energy and the hyperon content in the framework of relativistic mean-field models, following closely the work developed in Cavagnoli et al. (2011) and Providencia and Rabhi (2013), but with the care of choosing hyperonic models that have been calibrated to the existing experimental hypernuclei data, as developed in Fortin et al. (2017) . Besides, we will only consider unified inner crust-core EoS since a non-unified EoS may give rise to a large uncertainty on the star radius, as discussed in Fortin et al. (2016b).

The possible existence of hyperons inside NSs has been questioned (Demorest et al., 2010; Vidana et al., 2011) because many of the models including hyperons are not able to predict massive stars such as the pulsars PSR J1614 − 2230 (Demorest et al., 2010; Arzoumanian et al., 2018) and PSR J0348 + 0432 (Antoniadis et al., 2013) both with a mass close to or just above two solar masses, or even the PSR J1903 + 0327 with a mass 1.67 ±0.02$M_\odot$ (Freire et al., 2011; Vidana et al., 2011). This has been designated by the "hyperon puzzle" and a review of the problem, and of the solutions that can overcome possible contradictory scenarios has been presented in Chatterjee and Vidaña (2016). We will consider that the presence of hyperons is not simply ruled out by the existence of two solar mass stars and that this problem can be controlled by either using EoSs that are hard enough at high densities (Fortin et al., 2016b) or by going beyond the simple $SU(6)$ symmetry ansatz to fix the isoscalar vector meson couplings (Weissenborn et al., 2012, 2013). Other strategies have been suggested as considering hyperon-scalar-meson couplings weaker than the ones predicted by the SU(6) symmetry (Colucci and Sedrakian, 2013; van Dalen et al., 2014), or that nuclear matter may undergo a phase transition to quark matter (Alford et al., 2007, 2013; Weissenborn et al., 2011; Bonanno and Sedrakian, 2012; Klähn et al., 2013; Logoteta et al., 2013; Masuda et al., 2013; Zdunik and Haensel, 2013; Drago et al., 2016; Fukushima and Kojo, 2016; Pereira et al., 2016; Alford and Sedrakian, 2017). Having this in mind we will explore different RMF models of nuclear matter that satisfy a

set of well-established nuclear matter properties at saturation as developed in Fortin et al. (2016b).

The paper is organized in the following way: a review of the formalism and presentation of the models that will be used in the study is given in section 2. In sections 3, 4, we discuss, respectively, the calculation of the inner crust EoS, and the choice of the hyperon-meson couplings, including the calibration of the hyperon Λ-meson couplings for the recently proposed RMF models FSU2 (Chen and Piekarewicz, 2014), FSU2R, and FSU2H (Tolos et al., 2017). In section 5 the effect of the symmetry energy on the nucleonic direct Urca process, also in the presence of hyperons, and the effect of the still-badly constrained Σ-potential in symmetric nuclear matter on the star properties, including cooling, are discussed. Finally, in section 6 some conclusions are drawn.

2. THE MODEL

We will undertake the following discussion in the framework of a relativistic mean field (RMF) approach to the equation of state of nuclear and stellar matter. Many models have been proposed within this framework, see the recent publication (Dutra et al., 2014) for a compilation of a large number of those models and their properties. We will restrict ourselves to a small set of models and will consider two distinct classes of models: (a) models with density dependent baryon-meson couplings that avoid self-interacting or mixed terms between mesons and which will be designate by DD models; (b) models with constant baryon-meson couplings and which include non-linear meson terms in order to describe correctly properties of nuclei and nuclear matter, designated by NL models. Within this approach, we start from a Lorentz-covariant Lagrangian which describes baryons interacting with mesons. It is assumed the minimal coupling between the baryons and the mesons. We write the effective Lagrangian density in terms of three contributions,

$$\mathscr{L} = \mathscr{L}_b + \mathscr{L}_m + \mathscr{L}_{m-nl}, \qquad (1)$$

where $\mathscr{L}_b$ describes the baryons and their interaction with the mesons, the second term refers to the free Lagrangian density for the meson fields $\mathscr{L}_m$, both terms are included in DD and NL models. The third term, $\mathscr{L}_{m-nl}$, is only present in NL models and includes all the self-interaction terms between mesons and non-linear terms mixing two different mesons. The first term is given by

$$\mathscr{L}_b = \sum_{j=1}^{8} \bar{\psi}_j \left(i\gamma_\mu \partial^\mu - m_j + g_{\sigma j}\sigma + g_{\sigma^* j}\sigma^* \right.$$
$$\left. - g_{\omega j}\gamma_\mu \omega^\mu - g_{\phi j}\gamma_\mu \phi^\mu - g_{\rho j}\gamma_\mu \vec{\rho}^\mu \vec{I}_j \right) \psi_j. \qquad (2)$$

ψ_j stands for the field of j baryon, σ, σ^* are scalar-isoscalar meson fields, coupling to all baryons (σ) and to strange baryons (σ^*), and $\omega^\mu, \phi^\mu, \vec{\rho}^\mu$ denote the vector isoscalar (the first two) and isovector (the last) fields, respectively. The ω and $\vec{\rho}$ couple to all

baryons and the ϕ only to baryons with strangeness. The second term is given by

$$
\begin{aligned}
\mathcal{L}_m = &+\frac{1}{2}(\partial_\mu \sigma \partial^\mu \sigma - m_\sigma^2 \sigma^2) + \frac{1}{2}(\partial_\mu \sigma^* \partial^\mu \sigma^* - m_{\sigma*}^2 \sigma^{*2}) \\
&-\frac{1}{4}W_{\mu\nu}W^{\mu\nu} - \frac{1}{4}P_{\mu\nu}P^{\mu\nu} - \frac{1}{4}\vec{R}_{\mu\nu}\vec{R}^{\mu\nu} \\
&+\frac{1}{2}m_\omega^2 \omega_\mu \omega^\mu + \frac{1}{2}m_\phi^2 \phi_\mu \phi^\mu + \frac{1}{2}m_\rho^2 \vec{\rho}_\mu \cdot \vec{\rho}^\mu ,
\end{aligned}
\tag{3}
$$

where $W_{\mu\nu}, P_{\mu\nu}, \vec{R}_{\mu\nu}$ are the vector meson field tensors $V_{\mu\nu} = \partial_\mu V_\nu - \partial_\nu V_\mu$. Finally, the third term, that is only present in NL models, has the form

$$
\begin{aligned}
\mathcal{L}_{m-nl}(\sigma, \omega_\mu \omega^\mu) = &-\frac{1}{3}g_2 \sigma^3 - \frac{1}{4}g_3 \sigma^4 + \frac{1}{4}c_3 (\omega_\mu \omega^\mu)^2 \\
&+ \left(a_1 g_{\sigma N}^2 \sigma^2 + b_1 g_{\omega N} \omega_\mu \omega^\mu \right) \vec{\rho}_\mu \cdot \vec{\rho}^\mu \\
= &-U_s(\sigma) + U_v(\omega^\mu \omega_\mu) + A(\sigma, \omega^\mu \omega_\mu)\vec{\rho}_\mu \cdot \vec{\rho}^\mu .
\end{aligned}
\tag{4}
$$

These terms allow the reproduction of nuclear properties in NL models, and, in particular, the last term defines the density dependence of the symmetry energy.

For DD models, $\mathcal{L} = \mathcal{L}_b + \mathcal{L}_m$, and the couplings $g_{\sigma N}$, $g_{\omega N}$, $g_{\rho N}$ are functions of the baryonic density. The couplings of meson i to baryon j are written in the form

$$
g_{ij}(n_B) = g_{ij}(n_0)h_M(x) , \quad x = n_B/n_0 ,
\tag{5}
$$

where the density n_0 is the saturation density $n_0 = n_{sat}$ of symmetric nuclear matter. In the present study, we consider the parametrizations DD2 (Typel et al., 2010) and DDME2 (Lalazissis et al., 2005). For these two parametrizations the functions h_M assume for the isoscalar couplings the form (Typel et al., 2010),

$$
h_M(x) = a_M \frac{1 + b_M(x + d_M)^2}{1 + c_M(x + d_M)^2}
\tag{6}
$$

and for the isovector couplings the form

$$
h_M(x) = \exp[-a_M(x - 1)] .
\tag{7}
$$

The values of the parameters a_M, b_M, c_M, and d_M, as well as the σ, ω, and ρ meson masses, can be obtained from Typel et al. (2010) for DD2 and from Lalazissis et al. (2005) for DDME2.

For the class of NL models, we take the full Lagrangian density (1) and the constants couplings $g_{\sigma N}$, $g_{\omega N}$, $g_{\rho N}$, g_2, g_3, c_3, a_1, b_1 together with the σ, ω, and ρ meson masses are fitted to different kinds of data: experimental, theoretical and observational. We will only consider $a_1 \neq 0$ and $b_1 = 0$ or, $a_1 = 0$ and $b_1 \neq 0$. These terms have been introduced in Horowitz and Piekarewicz (2001a) and Horowitz and Piekarewicz (2001b) to explicitly model the density dependence of the symmetry energy.

Both classes of models will be considered in the mean field approximation, where the meson fields

are replaced by their respective expectation values in uniform matter:

$$
m_\sigma^2 \bar{\sigma} = \sum_{j \in B} g_{\sigma j} n_j^s + \frac{\partial \mathcal{L}_{m-nl}}{\partial \bar{\sigma}}
\tag{8}
$$

$$
m_{\sigma*}^2 \bar{\sigma}^* = \sum_{j \in B} g_{\sigma* j} n_j^s
\tag{9}
$$

$$
m_\omega^2 \bar{\omega} = \sum_{j \in B} g_{\omega j} n_j - \frac{\partial \mathcal{L}_{m-nl}}{\partial \bar{\omega}}
\tag{10}
$$

$$
m_\phi^2 \bar{\phi} = \sum_{j \in B} g_{\phi j} n_j
\tag{11}
$$

$$
m_\rho^2 \bar{\rho} = \sum_{j \in B} g_{\rho j} t_{3j} n_j - \frac{\partial \mathcal{L}_{m-nl}}{\partial \bar{\rho}}
\tag{12}
$$

with $\bar{\rho} = \langle \rho_3^0 \rangle$, $\bar{\omega} = \langle \omega^0 \rangle$, $\bar{\phi} = \langle \phi^0 \rangle$, and t_{3j} the third component of isospin of baryon j with the convention $t_{3p} = 1/2$. The scalar density of baryon j is given by

$$
n_j^s = \langle \bar{\psi}_j \psi_j \rangle = \frac{1}{\pi^2} \int_0^{k_{Fj}} k^2 \frac{M_j^*}{\epsilon_j} dk ,
\tag{13}
$$

and the number density by

$$
n_j = \langle \bar{\psi}_j \gamma^0 \psi_j \rangle = \frac{k_{Fj}^3}{3\pi^2} ,
\tag{14}
$$

where $\epsilon_j(k) = \sqrt{k^2 + M_j^{*2}}$, and effective chemical potential is

$$
\mu_j^* = \sqrt{k_{Fj}^2 + M_j^{*2}}.
\tag{15}
$$

The effective baryon mass M_i^* is expressed in terms of the scalar mesons

$$
M_i^* = M_i - g_{\sigma i}\bar{\sigma} - g_{\sigma* i}\bar{\sigma}^* ,
\tag{16}
$$

where M_i is the vacuum mass of the baryon i. The chemical potentials are defined by

$$
\mu_i = \mu_i^* + g_{\omega i}\bar{\omega} + g_{\rho i} t_{3i}\bar{\rho} + g_{\phi i}\bar{\phi} + \Sigma_0^R .
\tag{17}
$$

where the rearrangement term Σ_0^R is only present in the class of DD models and ensures thermodynamic consistency,

$$
\begin{aligned}
\Sigma_0^R = \sum_{j \in B} \Bigg(&\frac{\partial g_{\omega j}}{\partial n_j}\bar{\omega} n_j + t_{3j}\frac{\partial g_{\rho j}}{\partial n_j}\bar{\rho} n_j + \frac{\partial g_{\phi j}}{\partial n_j}\bar{\phi} n_j \\
&- \frac{\partial g_{\sigma j}}{\partial n_j}\bar{\sigma} n_j^s - \frac{\partial g_{\sigma* j}}{\partial n_j}\bar{\sigma}^* n_j^s \Bigg) .
\end{aligned}
\tag{18}
$$

In the class of DD models we consider the models DD2 (Typel et al., 2010) and DDME2 (Lalazissis et al., 2005). In the class of NL models we choose FSU2 (Chen and Piekarewicz, 2014), FSU2H and FSU2R (Tolos et al., 2017; Negreiros et al., 2018), NL3 (Lalazissis et al., 1997), NL3 $\sigma\rho$ and NL3 $\omega\rho$ (Horowitz and

TABLE 1 | Nuclear matter properties of the models considered in this study: saturation density n_0, binding energy B, incompressibility K, symmetry energy E_{sym}, and its slope L, all defined at saturation density, and the crust-core transition density n_t.

	n_0 [fm^{-3}]	B [MeV]	K [MeV]	E_{sym} [MeV]	L [MeV]	n_t [fm^{-3}]
DD MODELS						
DD2	0.149	−16.0	242.6	31.7	55	0.067
DDME2	0.152	−16.1	250.9	32.3	51	0.072
NL MODELS						
FSU2	0.1505	−16.28	238	37.6	113	0.054
FSU2R	0.1505	−16.28	238	30.7	47	0.083
FSU2H	0.1505	−16.28	238	30.5	44.5	0.087
NL3	0.148	−16.24	271	37.4	118	0.055
NL3 $\sigma\rho$	0.148	−16.24	271	31.7	55	0.080
NL3$\omega\rho$	0.148	−16.24	271	31.5	55	0.081
TM1	0.145	−16.26	281	36.8	108	0.060
TM1$\omega\rho$	0.145	−16.26	280	31.6	56	0.082
TM1 $\sigma\rho$	0.145	−16.26	280	31.4	56	0.080
TM1-2	0.145	−16.3	281.3	36.9	111	0.061
TM1-2 $\omega\rho$	0.146	−16.3	281.7	32.1	55	0.076

Piekarewicz, 2001a; Pais and Providência, 2016), TM1 (Sugahara and Toki, 1994), TM1$\omega\rho$ and TM1$\sigma\rho$ (Bao and Shen, 2014; Pais and Providência, 2016), TM1-2 and TM1-2 $\omega\rho$ (Providencia and Rabhi, 2013). See **Table 1** for their properties.

Most of these models have a symmetry energy slope below 60 MeV but there are three of them with a slope above 100 MeV (NL3, TM1, and FSU2), out of the range of values $40 < L < 62$ MeV (Lattimer and Lim, 2013) and $30 < L < 86$ MeV (Oertel et al., 2017) which where defined by terrestrial, theoretical, and, for the second range, also by observational constraints. In addition, these three models do not satisfy constraints obtained from microscopic calculations of neutron matter based on nuclear interactions derived from chiral effective field theory (Hebeler et al., 2013), or from realistic two- and three-nucleon interactions using quantum Monte Carlo techniques (Gandolfi et al., 2012). We keep them in the discussion because they are still frequently used and it is interesting to show how a stiff symmetry energy affects the behavior of an hyperonic EoS. Besides, the Lead Radius Experiment ("PREX") (Abrahamyan et al., 2012) has not excluded large symmetry energy slopes and models as the TAMUC parametrizations (Fattoyev and Piekarewicz, 2013) or the FSU2 parametrization (Chen and Piekarewicz, 2014) reproduce finite nuclei properties and the neutron star maximum mass, and have a similar slope or even larger. Also, from the analysis of elliptic flow in heavy ion-collisions the constraint $L = 85 \pm 22(exp) \pm 20(th) \pm 12(sys)$ MeV has been recently extracted (Cozma, 2018), and it does not exclude large slopes.

3. INNER CRUST

In the present study we will only consider unified EoSs at the level of the inner crust and core, since it has been shown in

Fortin et al. (2016b) Pais and Providência (2016) that a non-unified EoS may give rise to large uncertainties in the NS radius. In fact, if the inner crust EoS is not obtained consistently with the core EoS, that is using the same nuclear model, uncertainties on the radius determination may arise both due to the EoS chosen and to the matching procedure, in particular, the density chosen for the inner-crust core transition. The uncertainties introduced when using a non-consistent EoS for the core and the crust are larger for the less massive stars and, in Fortin et al. (2016b), it was shown that they can be as high as 4 and 30%, respectively, for the radius and crust thickness of a $1.0 M_{\odot}$ NS. In Pais and Providência (2016), the authors propose that, if the crust-core transition density is known , and it can be estimated from a dynamical spinodal calculation, an adequate choice of the inner crust EoS is to take one from a model that has a similar density dependence of the symmetry energy. In Zdunik et al. (2017) a simple and yet very accurate approximation is presented that allows to calculate with a high precision the NS radius and the crust thickness without employing any EoS for the crust. Several outer crust EoS are available presently, e.g., BPS, HP, or Ruester etc. (Baym et al., 1971; Haensel and Pichon, 1994; Rüster et al., 2006), but since they all are strongly constrained by nuclear physics data, the radius of the star is not affected by the choice of a particular one. It is important to stress that the inner crust EoS will affect the radius but not the mass of the star since the mass fraction in the crust is very small. On the other hand, the crust forming the less compact part of the star, it has an important contribution to the star total radius.

The inner crust EoSs for the models we are considering have been calculated within the Thomas-Fermi approximation (Avancini et al., 2008; Grill et al., 2012, 2014). In the above approach, we assume that the inner crust is formed by non-homogeneous npe matter inside a Wigner-Seitz cell of one, two, or three dimensions. Besides, the fields are considered to vary slowly so that matter can be treated as locally homogeneous. Since the density of the nucleons is determined by their Fermi momenta, we can then write the energy as a functional of the density. The equations of motion for the meson fields follow from variational conditions and are integrated over the whole cell. For a given density, the equilibrium configuration is the one that minimizes the free energy. For the present study, we have calculated the inner crust EoS for the models FSU2 (Chen and Piekarewicz, 2014) and FUS2R, FSU2H (Tolos et al., 2017) see **Table 5**. In **Table 2**, we give the density transitions between pasta configurations, n_{d-r} from droplets to rods and n_{r-s} from rods to slabs, as well as n_t, the crust-core transition density that defines the transition to homogeneous matter. β-equilibrium is imposed, and under these conditions, the configurations corresponding to tubes and bubbles are not present. We confirm the conclusion drawn in Oyamatsu and Iida (2007), where it was discussed that models with large values of L, such as FSU2, do not predict the existence of pasta phases, due to their large neutron skin thicknesses, contrary to models with a small value of L, such as FSU2R and FSU2H. In **Figure 5** we list the inner crust EoS, i.e., baryonic density, energy density ,and pressure, for the models FSU2, FSU2H, and FSU2R.

TABLE 2 | Density transitions in the pasta phase, n_{d-r} and n_{r-s}, for the models considered in this work.

Model	n_{d-r}	n_{r-s}	n_t
FSU2	–	–	0.054
FSU2R	0.037	0.060	0.083
FSU2H	0.041	0.067	0.087

n_t indicates the transition density to homogeneous matter. All densities are given in units of fm^{-3}.

4. CALIBRATED HYPERON COUPLINGS

In the present study, we will only consider calibrated Λ-meson couplings as obtained in Fortin et al. (2017, 2018a) in order to reproduce experimental data of Λ-hypernuclei. The binding energies of single and double Λ-hypernuclei are calculated solving the Dirac equations for the nucleons and Λs, following the approach described in Shen et al. (2006) and Avancini et al. (2007). For the RMF models with density-dependent couplings, we have assumed the same density dependence for hyperon- and nucleon-meson couplings.

Besides the hyperon-meson coupling calibration to the hypernuclei properties done in Shen et al. (2006), some other works have discussed this problem. Glendenning and Moszkowski (1991) have been the first to set constraints on the scalar and vector couplings of the hyperons using hypernuclei measurements, in particular, the empirical binding of the Λ hyperon in saturated symmetric nuclear matter. More recently van Dalen et al. (2014) have adjusted a relativistic density functional to simultaneaously satisfy laboratory hypernuclei data and astronomical data, allowing SU(6) symmetry breaking and mixing in the isoscalar sector.

Following the approach described in Fortin et al. (2017), we have obtained calibrated couplings for the FSU2 (Chen and Piekarewicz, 2014), and the FSU2R and FSU2H RMF parametrizations recently proposed in Tolos et al. (2017). The last two parametrizations have been fitted to both properties of nuclear matter and finite nuclei and NS properties. The former one was fitted to ground-state properties of finite nuclei and their monopole response. They all describe $2M_\odot$ NSs.

The values of the coupling constant fractions $R_{\sigma\Lambda}$ and $R_{\omega\Lambda}$ to the σ and ω mesons are given in **Table 3**, and $R_{\sigma^*\Lambda}$ and $R_{\phi\Lambda}$ to the σ^* and ϕ mesons in **Table 4** where $R_{\sigma\Lambda} = g_{\sigma\Lambda}/g_{\sigma N}$ and similarly for the other meson fields. For reference, we also give the Λ-potential in symmetric nuclear matter at saturation density n_0 in **Table 3**, and in pure Λ-matter at n_0 and $n_0/5$ in **Table 4** as these are quantities traditionally used to obtain hyperonic EoSs within the RMF approach.

For the coupling of the Λ to the ω meson we consider either the $SU(6)$ quark model value: $R_{\omega\Lambda}(SU(6)) = 2/3$, the so-called models "-a," or the maximum expected coupling, i.e., $R_{\omega\Lambda} = 1$, forming the models "-b." For the coupling between the Λ and the ϕ-meson we include in the tables results obtained with the $SU(6)$ value, $R_{\phi\Lambda}(SU(6)) = -\sqrt{2}/3$ and with $3R_{\phi\Lambda}(SU(6))/2 = -\sqrt{2}/2$. We assume that the ω and ϕ mesons do not couple (Schaffner and Mishustin, 1996; Weissenborn et al., 2012).

TABLE 3 | Calibration to single Λ-hypernuclei: for given $R_{\omega\Lambda}$, values of $R_{\sigma\Lambda}$ calibrated to reproduce the binding energies B_Λ of hypernuclei in the s and p shells.

Model	$R_{\omega\Lambda}$	$R_{\sigma\Lambda}$	$U_\Lambda^N(n_0)$
FSU2-a	2/3	0.619	−30
FSU2-b	1	0.894	−32
FSU2R-a	2/3	0.618	−34
FSU2R-b	1	0.893	−37
FSU2H-a	2/3	0.620	−35
FSU2H-b	1	0.893	−38

The last column contains the value of the Λ-potential in symmetric baryonic matter at saturation in MeV, for reference.

For a given ϕ-meson coupling, the σ^*-meson coupling is fitted to the bond energy of the only double-Λ hypernucleus for which it has been measured unambiguously, that is $^{6}_{\Lambda\Lambda}$He. Two sets of parameters are given for each ϕ coupling corresponding to the lower and upper values of the bond energy of $^{6}_{\Lambda\Lambda}$He: $\Delta B_{\Lambda\Lambda} = 0.50$ or 0.84 MeV.

To test the new parametrizations, we have integrated the Tolman-Oppenheimer-Volkoff equations, allowing the appearance of hyperons in the core of the star. For the outer crust, we have considered the EoS proposed in Rüster et al. (2006), and the EoS of the inner crust was obtained from a Thomas Fermi calculation, see (Grill et al., 2012, 2014), as discussed in the previous section, consistently with the core EoS.

With the complete EoS, we have calculated the NS maximum mass $M_{\max}$ as a function of $R_{\phi\Lambda}$ including only the Λ hyperons in the EoS in addition to the nucleons, for the models "-a" and "-b," see black lines in **Figure 1**. The values $R_{\sigma\Lambda}$, $R_{\phi\Lambda}$, and $R_{\sigma^*\Lambda}$ are adjusted to reproduce the binding energies of single Λ-hypernuclei and of $^{6}_{\Lambda\Lambda}$He with $\Delta B_{\Lambda\Lambda} = 0.50$ MeV (solid lines) and 0.84 MeV (dashed lines).

In **Figure 1** the colored lines correspond to models that also include the Ξ and Σ hyperons. For these hyperons the values of hyperonic single-particle mean field potentials have been used to constrain the scalar coupling constants. The potential for a hyperon Y in symmetric nuclear matter is given by

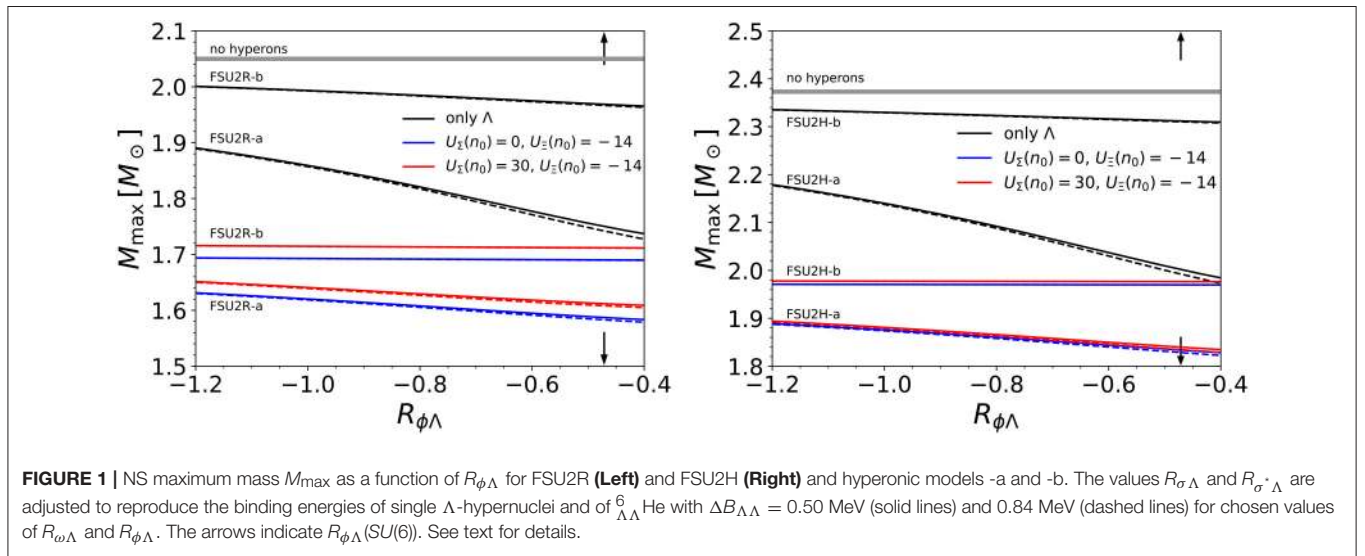$$U_Y^N(n_k) = M_Y^* - M_Y + \mu_Y - \mu_Y^*, \tag{19}$$

where the chemical potential μ_Y and the effective chemical potential μ_Y^* have been defined in Equations (17) and (15). For the Ξ potential we take $U_\Xi^N(n_0) = -14$ MeV, compatible with the analysis in Khaustov et al. (2000) and Gal et al. (2016) of the experimental data for the reaction ^{12}C$(K^-, K^+)^{12}_\Xi$Be, which are reproduced using a potential $U_\Xi^N(n_0) \sim -14$ to -18 MeV.

Phenomenological analysis of data on Σ^- atoms and (π^-, K^+) reactions indicate that the Σ potential in nuclear matter is repulsive and strongly spin dependent (Gal, 2010; Sugimura et al., 2014; Gal et al., 2016; Honda et al., 2017; Harada et al., 2018), an estimation for the isoscalar Σ-potential at saturation density being $+30 \pm 20$ MeV. Similar conclusions are drawn for the Σ-nucleon potential derived within the chiral effective field theory Haidenbauer and Meißner (2015), although

TABLE 4 | Calibration to double Λ-hypernuclei for models -a and -b of **Table 3**.

Model	$R_{\phi\Lambda}$	$\Delta B_{\Lambda\Lambda} = 0.50$			$\Delta B_{\Lambda\Lambda} = 0.84$		
		$R_{\sigma^*\Lambda}$	$U_\Lambda^\Lambda(n_0)$	$U_\Lambda^\Lambda(n_0/5)$	$R_{\sigma^*\Lambda}$	$U_\Lambda^\Lambda(n_0)$	$U_\Lambda^\Lambda(n_0/5)$
FSU2-a	$-\sqrt{2}/3$	0.553	−7.98	−5.03	0.577	−11.33	−5.72
	$-\sqrt{2}/2$	0.862	−5.56	−5.04	0.877	−8.88	−5.74
FSU2-b	$-\sqrt{2}/3$	0.573	0.48	−6.21	0.604	−3.85	−7.15
	$-\sqrt{2}/2$	0.874	5.39	−6.18	0.894	1.15	−7.12
FSU2R-a	$-\sqrt{2}/3$	0.552	−7.52	−4.95	0.577	−11.00	−5.67
	$-\sqrt{2}/2$	0.860	−5.12	−4.96	0.876	−8.56	−5.68
FSU2R-b	$-\sqrt{2}/3$	0.573	1.31	−6.15	0.604	−3.13	−7.11
	$-\sqrt{2}/2$	0.873	6.18	−6.12	0.894	1.83	−7.08
FSU2H-a	$-\sqrt{2}/3$	0.544	−8.62	−5.52	0.570	−12.16	−6.26
	$-\sqrt{2}/2$	0.848	−6.42	−5.53	0.865	−9.93	−6.26
FSU2H-b	$-\sqrt{2}/3$	0.564	4.20	−7.01	0.598	−0.34	−7.99
	$-\sqrt{2}/2$	0.860	8.75	−6.98	0.883	4.31	−7.96

For a given $R_{\phi\Lambda}$, $R_{\sigma^*\Lambda}$ is calibrated to reproduce either the upper or the lower values of bound energy of $^6_{\Lambda\Lambda}$He. For reference the Λ-potential in pure Λ-matter at saturation and at $n_0/5$ are also given. All energies are given in MeV.

FIGURE 1 | NS maximum mass M_{max} as a function of $R_{\phi\Lambda}$ for FSU2R **(Left)** and FSU2H **(Right)** and hyperonic models -a and -b. The values $R_{\sigma\Lambda}$ and $R_{\sigma^*\Lambda}$ are adjusted to reproduce the binding energies of single Λ-hypernuclei and of $^6_{\Lambda\Lambda}$He with $\Delta B_{\Lambda\Lambda} = 0.50$ MeV (solid lines) and 0.84 MeV (dashed lines) for chosen values of $R_{\omega\Lambda}$ and $R_{\phi\Lambda}$. The arrows indicate $R_{\phi\Lambda}(SU(6))$. See text for details.

slightly less repulsive potentials are predicted, of the order of +15 MeV. Taking into account the existing uncertainties with respect to the strength of the Σ potential we show results for two values, $U_\Sigma^N(n_0) = 0$ and +30 MeV.

Since, presently no information on double Ξ- or Σ-hypernuclei exist, we obtain a lower limit for the maximum mass of hyperonic NSs not including the mesons that account for the YY interaction except for the Λ-hyperons in order to reproduce measurements obtained for $^6_{\Lambda\Lambda}$He. However, since the ϕ meson is responsible for a repulsive YY interaction, its inclusion will raise the lower mass limit favoring more massive stars. In the next section, we will, therefore, perform our discussion including the ϕ-meson and will fix its coupling using SU(6) symmetry arguments. For the ω-meson couplings we consider the SU(6) values:

$$g_{\omega\Xi} = \frac{1}{3}g_{\omega N} = \frac{1}{2}g_{\omega\Sigma}. \tag{20}$$

In **Figure 1** predictions for two limiting scenarios are plotted: (a) the EoSs defining the minimal hyperonic model include only the Λ hyperons in addition to the nucleons (black lines). These models may be considered to set an upper limit on the maximum mass of an hyperonic NS, because adding other degrees of freedom will soften the EoS; (b) the EoSs designated as maximal hyperonic models include the full baryonic octet (colored lines). An estimation of the lower limits for the maximum mass of hyperonic NSs is obtained not including the mesons that account for the YY interaction. The blue stripped areas in **Figure 2** correspond, precisely, to the mass range covered when employing the minimal hyperonic models and the maximal hyperonic models with $U_\Sigma(n_0) = 0$ MeV and $U_\Xi(n_0) = -14$ MeV, taking the SU(6) values of the coupling constants $R_{\omega\Lambda}$ and $R_{\phi\Lambda}$ for both sets of models and also the SU(6) value of the coupling constant $R_{\omega\Sigma}$ in the maximal hyperonic models.

TABLE 5 | Equation of state of the inner crust with pasta for the FSU2, FSU2R, and FSU2H models.

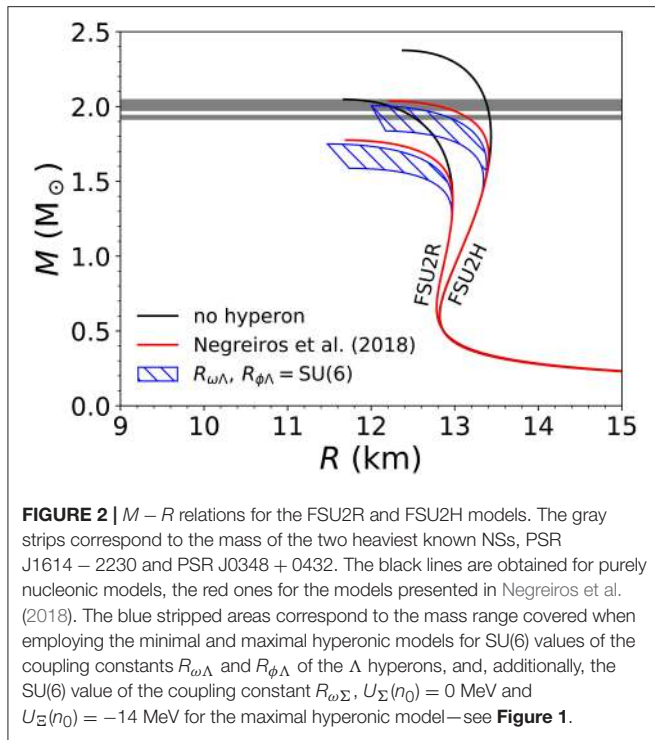| n_B (fm^{-3})	FSU2		FSU2R		FSU2H	
	ε	P	ε	P	ε	P
0.002	–	–	0.009527397342	1.114900624E-05	0.009527062997	1.084494306E-05
0.003	0.01427514106	1.190916646E-05	0.014298330992	1.92066982E-05	0.014297628775	1.854789298E-05
0.004	0.019038049504	1.555793278E-05	0.019072251394	2.883538582E-05	0.0190710444	2.77711606E-05
0.005	0.023801861331	1.90039882E-05	0.0238487795	3.988303797E-05	0.023846937343	3.831203867E-05
0.006	0.02856634371	2.219665839E-05	0.028627665713	5.224829874E-05	0.028625067323	5.00691749E-05
0.007	0.033331338316	2.518662041E-05	0.033408716321	6.588049291E-05	0.033405266702	6.304256385E-05
0.008	0.038096740842	2.787251651E-05	0.038191791624	8.06275857E-05	0.038187392056	7.702950097E-05
0.009	0.042862471193	3.045706035E-05	0.042976766825	9.633754962E-05	0.042971335351	9.21820174E-05
0.01	0.047628492117	3.299092714E-05	0.047763541341	0.0001129090306	0.047757018358	0.0001081453593
0.011	0.052394766361	3.547411325E-05	0.052552033216	0.0001304940524	0.052544362843	0.000125274295
0.012	0.057161271572	3.816001117E-05	0.057342153043	0.0001487378759	0.057333290577	0.0001430620323
0.013	0.061928000301	4.089658614E-05	0.062133830041	0.0001677418768	0.062123749405	0.0001618632959
0.014	0.066694952548	4.403857383E-05	0.06692700088	0.0001874553564	0.066915675998	0.0001813740673
0.015	0.071462139487	4.753530811E-05	0.071721583605	0.0002076755918	0.071709007025	0.0002014929632
0.016	0.076229587197	5.148813943E-05	0.076517544687	0.0002283012436	0.07650372386	0.0002223720076
0.017	0.080997288227	5.609977597E-05	0.08131480962	0.0002493830107	0.081299744546	0.0002436057839
0.018	0.08576527983	6.131953705E-05	0.0861133039	0.0002707181557	0.086097031832	0.0002654477139
0.019	0.090533591807	6.740081153E-05	0.090913005173	0.0002924080472	0.090895555913	0.0002876950603
0.02	0.09530223906	7.4292926E-05	0.095713868737	0.0003139965702	0.095695272088	0.0003102971241
0.021	0.100071251392	8.219858137E-05	0.100515827537	0.0003359398397	0.100496120751	0.0003333046334
0.022	0.104840673506	9.121913899E-05	0.105318851769	0.0003578324395	0.105298064649	0.0003565148218
0.023	0.109610520303	0.000101202575	0.11012288928	0.0003798264079	0.110101081431	0.0003796743404
0.024	0.114380836487	0.0001125542913	0.114927917719	0.0004017696483	0.114905133843	0.0004031886056
0.025	0.119151651859	0.0001250715868	0.119733855128	0.0004236115783	0.119710162282	0.0004268042394
0.026	0.123922996223	0.0001390585239	0.124540701509	0.0004456055467	0.124516174197	0.0004503185046
0.027	0.12869489193	0.0001543630642	0.129348397255	0.0004673461081	0.129323080182	0.0004739848082
0.028	0.133467406034	0.0001713399688	0.134156942368	0.000488934631	0.13413092494	0.0004976511118
0.029	0.138240531087	0.0001899385388	0.138966232538	0.0005105231539	0.138939589262	0.0005212160759
0.03	0.143014326692	0.0002100067359	0.143776282668	0.0005318076001	0.143749088049	0.0005448316806
0.031	0.147788822651	0.00023195002	0.148587062955	0.0005528387264	0.148559391499	0.0005683459458
0.032	0.152564063668	0.0002554136154	0.153398528695	0.0005738697946	0.153370469809	0.0005917081726
0.033	0.157340064645	0.0002810056321	0.158210650086	0.0005944954464	0.158182263374	0.0006148677203
0.034	0.162116870284	0.0003082193434	0.163023427129	0.0006149184192	0.162994787097	0.0006379765691
0.035	0.166894495487	0.000337612204	0.167836785316	0.0006351386546	0.167807996273	0.0006608827389
0.036	0.171672984958	0.0003686773998	0.172650724649	0.0006551561528	0.1726218611	0.0006836875109
0.037	0.176452368498	0.000402124424	0.177465245128	0.0006747682928	0.177436366677	0.0007060868666
0.038	0.181232705712	0.00043759853	0.182280123234	0.0006842956063	0.182251513004	0.0007283848827
0.039	0.1860139817	0.0004748970096	0.187095478177	0.0007031476125	0.187067225575	0.0007504802197
0.04	0.190796226263	0.0005146786571	0.191911309958	0.0007218982209	0.191883504391	0.0007723727613
0.041	0.195579528809	0.0005562847364	0.196727633476	0.0007402940537	0.196700364351	0.0007939613424
0.042	0.200363859534	0.0006004753523	0.201544389129	0.0007583858096	0.201517611742	0.0008047556039
0.043	0.205149263144	0.0006465410697	0.206361606717	0.000776224304	0.206335306168	0.0008256346337
0.044	0.209935769439	0.0006952419062	0.211179211736	0.0007938092458	0.21115347743	0.000846361625
0.045	0.214723423123	0.0007457671454	0.215997248888	0.0008110902854	0.215972140431	0.0008667845977
0.046	0.219512179494	0.0007990797167	0.220815643668	0.0008282191702	0.220791265368	0.0008869034355
0.047	0.224302142859	0.0008542166324	0.22563444078	0.000844891998	0.225610807538	0.0009068703512
0.048	0.229093328118	0.000912090065	0.230453595519	0.0008614128456	0.230430826545	0.0009265838307
0.049	0.233885720372	0.0009717879584	0.235273063183	0.0008776801988	0.235251218081	0.0009459425928
0.05	0.238679364324	0.001034171786	0.240092903376	0.0008935928927	0.24007204175	0.0009650985594

(Continued)

TABLE 5 | Continued

n_B (fm^{-3})	FSU2		FSU2R		FSU2H	
	ε	P	ε	P	ε	P
0.051	0.243474245071	0.001098278561	0.244913056493	0.0009093027911	0.244893237948	0.0009840012062
0.052	0.24827042222	0.001162892091	0.249733552337	0.0009247594862	0.249714821577	0.001002650475
0.053	0.25306776166	0.001220613485	0.2545543015	0.0009399626288	0.254536747932	0.001021046308
0.054	0.257866412401	0.001290649641	0.259375363588	0.0009549123934	0.259359031916	0.001039239462
0.055	–	–	0.2641967237	0.0009696595371	0.264181643724	0.001057128538
0.056	–	–	0.269018322229	0.0009840518469	0.269004613161	0.001074814936
0.057	–	–	0.273840218782	0.0009982922347	0.273827910423	0.001092247898
0.058	–	–	0.278662353754	0.001012228429	0.278651505709	0.00110942754
0.059	–	–	0.283484727144	0.001025962061	0.283475399017	0.001126353745
0.06	–	–	0.288307338953	0.001039492781	0.288299590349	0.001143077272
0.061	–	–	0.293129920959	0.001004930935	0.293124079704	0.001159547362
0.062	–	–	0.297952502966	0.001019424642	0.29794883728	0.001175764133
0.063	–	–	0.302775323391	0.001033664914	0.302773833275	0.001191778225
0.064	–	–	0.307598352432	0.001047702623	0.307599157095	0.001207640162
0.065	–	–	0.312421619892	0.001061537536	0.312424719334	0.001223147381
0.066	–	–	0.317245006561	0.001075220411	0.317250490189	0.001238451921
0.067	–	–	0.322068631649	0.001088599092	0.322076499462	0.001253503142
0.068	–	–	0.326892495155	0.001101825968	–	–
0.069	–	–	0.331716567278	0.001114748651	–	–
0.07	–	–	0.33654075861	0.001127468655	–	–
0.071	–	–	0.34136518836	0.001139935222	0.341381192207	0.001264145365
0.072	–	–	0.346189767122	0.00115209783	0.346207857132	0.001279652584
0.073	–	–	0.351014554501	0.00116395636	0.35103482008	0.001294906368
0.074	–	–	0.355839431286	0.001175460056	0.355861902237	0.001309957588
0.075	–	–	0.36066454649	0.001186609035	0.360689252615	0.001324755372
0.076	–	–	0.365489840508	0.001197352656	0.365516811609	0.001339299721
0.077	–	–	0.370315164328	0.001207538764	0.370344519615	0.001353590749
0.078	–	–	0.375140637159	0.001217218116	0.375172406435	0.001367526944
0.079	–	–	0.379966259003	0.001226238674	0.380000561476	0.001381159294
0.08	–	–	0.384792000055	0.001234499039	0.384828835726	0.001394436695
0.081	–	–	0.389617711306	0.001241948688	0.389657229185	0.00140725798
0.082	–	–	0.394443571568	0.001248486107	0.394485831261	0.001419521985
0.083	–	–	0.399269461632	0.0012539085	0.399314552546	0.001431279001
0.084	–	–	–	–	0.404143542051	0.001442377339
0.085	–	–	–	–	0.408972501755	0.001452614204
0.086	–	–	–	–	0.413801699877	0.001462040236
0.087	–	–	–	–	0.418630868196	0.001470199204

The energy density, ε, and pressure, P, are in units of fm^{-4}.

Under the above conditions the FSU2R model with hyperons does not describe two solar mass stars [not even 1.9 $M_\odot$ as indicated by the most recent measurements of PSR J1614 − 2230 (Arzoumanian et al., 2018)]. This conclusion had already been drawn in Tolos et al. (2017). In **Figure 2** the red curves have been obtained with the hyperon parametrization defined in Tolos et al. (2017). It lies above the upper limit defined by the minimal hyperonic model because the σ^* was not included, and the Λ-σ coupling was also smaller giving rise to a potential equal to –28 MeV instead of ∼ −35 MeV obtained with the calibrated parametrization.

5. SYMMETRY ENERGY AND HYPERONIC NEUTRON STARS

In the present section, we discuss the effect of the density dependence of the symmetry energy on the onset of the different hyperon species, and on the onset of the direct Urca process in the presence of hyperons. The study will be undertaken considering a family of models generated from the TM1 model (Sugahara and Toki, 1994). The inclusion of the non-linear term $\mathscr{L}_{nl}$ that couples the ω and the σ mesons to the ρ-meson will allow the generation of a family of models with the same underlying

FIGURE 2 | $M − R$ relations for the FSU2R and FSU2H models. The gray strips correspond to the mass of the two heaviest known NSs, PSR $J1614 − 2230$ and PSR $J0348 + 0432$. The black lines are obtained for purely nucleonic models, the red ones for the models presented in Negreiros et al. (2018). The blue stripped areas correspond to the mass range covered when employing the minimal and maximal hyperonic models for SU(6) values of the coupling constants $R_{\omega\Lambda}$ and $R_{\phi\Lambda}$ of the Λ hyperons, and, additionally, the SU(6) value of the coupling constant $R_{\omega\Sigma}$, $U_\Sigma(n_0) = 0$ MeV and $U_\Xi(n_0) = −14$ MeV for the maximal hyperonic model—see **Figure 1**.

isoscalar properties and different isovector properties (Bao and Shen, 2014; Pais and Providência, 2016). This family is built in such a way that all the models predict the same symmetry energy, equal to the one predicted by TM1, at $n_B = 0.1$ fm^{-3}. It was shown in Pais and Providência (2016) that the ground-state properties of nuclei used to calibrate TM1 are still quite well-reproduced when the new terms are introduced in the model. Contrary to the previous section, in the present and following sections we will consider that the Σ and Ξ hyperons couple to the ϕ-meson with the couplings defined by the $SU(6)$ symmetry, unless when **Figure 9** is discussed.

5.1. The Direct Urca Process: Nucleonic Neutron Stars

The most efficient cooling mechanism of a NS by neutrino emission is the nucleonic electron direct Urca (DU) process (Lattimer et al., 1991) described by the equations

$$n \to p + e^- + \bar{\nu}_e \quad \text{and} \quad p + e^- \to n + \nu_e. \quad (21)$$

This process operates only if momentum conservation is allowed, and this can be translated into the inequalities:

$$p_{Fn} \leq p_{Fp} + p_{Fe}, \quad (22)$$

where p_{Fi} is the Fermi momentum of species i. As a consequence, in order for the DU process to occur the proton fraction must be equal or above a minimum proton fraction Y_p^{min} (Klahn et al., 2006):

$$Y_p^{min} = \frac{1}{1 + \left(1 + x_e^{1/3}\right)^3}, \quad (23)$$

where $x_e = n_e / (n_e + n_\mu)$, and n_e and n_μ are the electron and muon densities. In the following, we will designate by n_{DU} and mass M_{DU}, respectively, the baryonic density at which the DU process sets in and the mass of the star where it starts operating, i.e., which has a central density equal to n_{DU}.

For some models the nucleonic DU process does not operate inside NSs because the onset DU density is above the central density of the most massive star. In our study this is the case for the two models with density-dependent coupling parameters DD2 and DDME2.

In order to discuss the influence of the density dependence of the symmetry energy on the DU process, we include in **Figure 3** right panel the DU onset density as a function of the slope L of the symmetry energy at saturation density (blue curves) and the corresponding star masses on the left panels. The blue dotted line is obtained for the nucleonic EoSs from the family of TM1 models defined in section 2 and the other blue curves have been obtained for hyperonic EoSs and will be discussed below. It is clear that the DU process is strongly influenced by the density dependence of the symmetry energy, because this quantity defines the proton fraction in matter. A similar relation was obtained in Cavagnoli et al. (2011) and Providência et al. (2014). A large symmetry energy disfavors a large proton-neutron asymmetry and, therefore, favors the DU process and it sets in at low densities. On the contrary, a small symmetry energy allows for large proton-neutron asymmetries hence pushing the DU threshold to higher densities. In Horowitz and Piekarewicz (2002), the authors have discussed how it is possible to establish a relation between the ^{208}Pb neutron skin and the possibility of occurring the DU process. Since the nuclear neutron skin is strongly correlated with the slope L, the above observation is equivalent to the one displayed in **Figure 3**.

5.2. The Direct Urca Process: Hyperonic Neutron Stars

In the presence of hyperons, other channels are opened for neutrino emission (Prakash et al., 1992):

$$\Sigma^- \to \Sigma^0 \ell^- \bar{\nu}_\ell, \quad R = 0.61 \quad (24)$$
$$\Xi^- \to \Xi^0 \ell^- \bar{\nu}_\ell, \quad R = 0.22 \quad (25)$$
$$\Sigma^- \to \Lambda \ell^- \bar{\nu}_\ell, \quad R = 0.21 \quad (26)$$
$$\Xi^0 \to \Sigma^+ \ell^- \bar{\nu}_\ell, \quad R = 0.06 \quad (27)$$
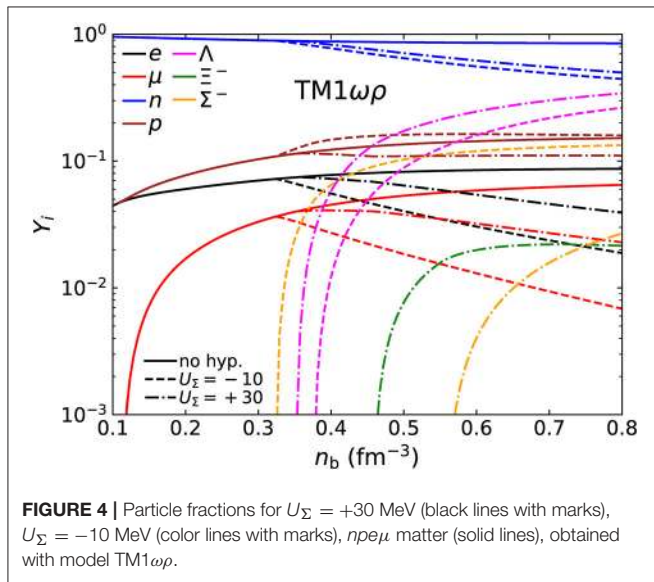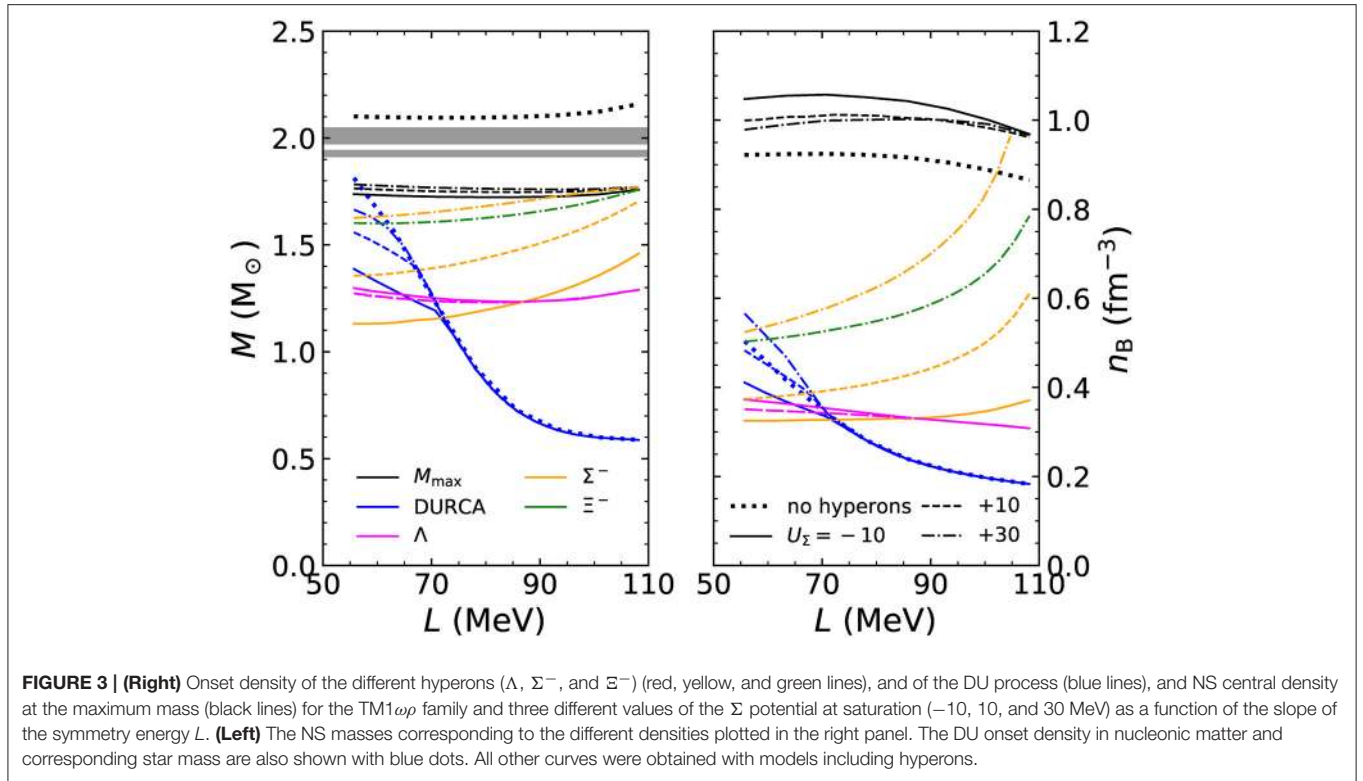$$\Lambda \to p \ell^- \bar{\nu}_\ell, \quad R = 0.04 \quad (28)$$
$$\Xi^- \to \Sigma^0 \ell^- \bar{\nu}_\ell, \quad R = 0.03 \quad (29)$$
$$\Xi^- \to \Lambda \ell^- \bar{\nu}_\ell, \quad R = 0.02 \quad (30)$$
$$\Sigma^- \to n \ell^- \bar{\nu}_\ell, \quad R = 0.01. \quad (31)$$

For each process the R factor indicates the efficiency of each process with respect to the nucleonic DU process for which $R = 1$ (see Prakash et al., 1992). These different hyperonic DU channels are opened as soon as the species involved set in. The most efficient processes being the ones described by Equations (24–26) and, in particular, the process (24) is almost three times more

FIGURE 3 | (Right) Onset density of the different hyperons (Λ, Σ^-, and Ξ^-) (red, yellow, and green lines), and of the DU process (blue lines), and NS central density at the maximum mass (black lines) for the TM1$\omega\rho$ family and three different values of the Σ potential at saturation (-10, 10, and 30 MeV) as a function of the slope of the symmetry energy L. **(Left)** The NS masses corresponding to the different densities plotted in the right panel. The DU onset density in nucleonic matter and corresponding star mass are also shown with blue dots. All other curves were obtained with models including hyperons.

FIGURE 4 | Particle fractions for $U_\Sigma = +30$ MeV (black lines with marks), $U_\Sigma = -10$ MeV (color lines with marks), $npe\mu$ matter (solid lines), obtained with model TM1$\omega\rho$.

efficient that the other two. This indicates that it is important to establish whether the Σ-hyperon occurs inside a NS. Since this hyperon has isospin equal to one, it is expected that its occurrence will be strongly influenced by the density dependence of the symmetry energy.

The occurrence of hyperons affects the neutron, proton and electron fractions. Therefore, Equation (21) for the nucleonic DU threshold looses validity, and after hyperons set in, the minimum

proton fraction for nucleonic electron DU is given by

$$\left(\frac{n_p}{n_p + n_n}\right) = \frac{1}{1 + \left(1 + x_e^{Y1/3}\right)^3}, \quad x_e^Y = \frac{n_e}{n_e + n_\mu - n_Y^{ch}},$$

(32)

where $n_Y^{ch} = -n_{\Sigma^-} + n_{\Sigma^+} - n_{\Xi^-}$. The nucleonic electron DU process is not affected by the presence of hyperons in models with a large slope L because its threshold is at densities lower than the hyperon onset density. However, if $L \leq 75$ MeV, the presence of hyperons will affect the nucleonic electron DU process and the effect depends on the value of the Σ potential: if very repulsive (U_Σ of the order of couple of tens of MeV), the DU process turns on at densities larger that the one obtained for nucleonic matter. The contrary holds for less repulsive Σ potentials.

In **Figure 4**, the fractions of the particles present inside a NS star below $n = 0.8$ fm^{-3} for the TM1$\omega\rho$ parametrization are shown for hyperon free matter (thin black lines) and for hyperonic matter taking $U_\Sigma(n_0) = -10$ and $+30$ MeV. For the attractive potential (U_Σ at saturation negative) the Σ^- is the first hyperon to set in and as soon as it appears the proton fraction increases and the neutron fraction decreases, reducing the difference between the proton and neutron Fermi momenta and favoring the DU process relative to nucleonic matter. For the very repulsive potential at saturation: $U_\Sigma = 30$ MeV, a value that is generally employed in the recent literature, the Λ is the first hyperon to set in and above its densities of appearance the fractions of neutrons, protons, electrons, and muons all suffer a reduction, the overall effect being that DU is disfavored with respect to nucleonic matter.

In **Figure 3** right panel, which was partially discussed before, we also plot, besides the onset density of the nucleonic electron DU process, the onset densities of the Λ, Σ^-, and Ξ^- hyperons, and the central density n_c of the NS with the maximum mass for three different values of U_Σ at saturation: -10, 10, and 30 MeV. Hyperons that are not included in the figure do not appear at densities below n_c and hence are not present at all in NSs. The gray bands show the mass constraints set by the pulsars PSR J1614 $-$ 2230 and PSR J0348 $+$ 0432. Even though the TM1$\omega\rho$ family with hyperons and the vector meson couplings to the hyperons defined by the $SU(6)$ symmetry do not satisfy the two solar mass constraint, the main conclusions drawn with respect to the L dependence of the several properties we discuss, is still valid for more massive stars.

For $L \geq 75$ MeV the DU process sets in at a density below the hyperon onset density and, in fact, the DU process is possible at densities of the order of $2n_0$ or below, corresponding to stars with a mass equal to $1M_\odot$ or below. Observations do not support a fast cooling for these low masses (see e.g., discussion in Fortin et al., 2018b). The DU mass threshold rises monotonously as L decreases below 75 MeV, and for $L = 50$ MeV attains $1.4 - 1.7M_\odot$ depending on the value of U_Σ, a large repulsive value favoring a higher threshold. Similar conclusions have been drawn in Cavagnoli et al. (2011), although using different hyperonic models.

We finally comment on the effect of L on the hyperonic species inside the star. The Λ hyperon onset is practically not affected by the value of U_Σ, and, although its onset density increases slightly when L decreases, the mass of star at the Λ-onset is essentially independent of L and equal to $1.3M_\odot$. However, the other two hyperons Σ^- and Ξ^-, having a non-zero isospin are strongly affected by the density dependence of the symmetry energy, the onset density decreasing as L decreases. The more repulsive the U_Σ the larger the onset density of the Σ and the mass of the star where the hyperon sets in.

The strongest effect of the $U_\Sigma(n_0)$ is observed for the lowest values of L. At $L = 56$ MeV in nucleonic matter, the DU sets in at $n_{DU} = 0.504$ fm^{-3} corresponding to a star with a mass $M_{DU} = 1.81\,M_\odot$. The density n_{DU} and mass M_{DU} change to $n_{DU} = 0.411$ fm^{-3} and $M_{DU} = 1.39\,M_\odot$ if $U_\Sigma(n_0) = -10$ MeV, and to $n_{DU} = 0.566$ fm^{-3} and $M_{DU} = 1.67\,M_\odot$ if $U_\Sigma(n_0) = +30$ MeV, The Ξ^- does not occur unless the Σ potential is quite repulsive.

One fact that should be pointed out is that the overall effect of the value of L on the star maximum mass is negligible, a conclusion that had already been drawn in Cavagnoli et al. (2011) and Providencia and Rabhi (2013).

Next, we would like to quantify the effect of strangeness on the star radius. This will be achieved by calculating the total strange baryonic fraction N_S/N_B in stars with a fixed mass and comparing the radii of these stars. N_S is the star total strange baryonic number and is defined by

$$N_S = \frac{4\pi}{3} \int_0^R dr \frac{n_s r^2}{\sqrt{1 - m(r)/r}},$$

FIGURE 5 | **(Left)** Radius of a $1.67M_\odot$ NS as a function of the total strange baryonic fraction N_S/N_B at the maximum mass for four TM1$\omega\rho$ models with four different values of the slope L: 55.7, 68.0, 84.8, and 108.2 MeV. **(Right)** M-R curves obtained with the models with the different values of L for $U_\Sigma = +30$ MeV (thick lines) and -10 MeV (thin lines). The line color indicates the value of the L as in the left panel. The blue upper bands show the constraints set by the pulsars PSR J1614 $-$ 2230 and PSR J0348 $+$ 0432.

where $m(r)$ is the mass inside the radius r and n_s the magnitude of the strangeness density, and N_B is the total baryonic number of the star. As reference mass, we take a mass equal to $1.67M_\odot$, the mass of the pulsar PSR J1903+0327, because the onset of strangeness generally occurs in stars with a mass below this value. In **Figure 5** left panel, we show how the radius of NSs with a mass equal to $1.67M_\odot$ changes with the total strange baryonic fraction N_S/N_B when U_Σ varies between -10 and $+30$ MeV and the other hyperon coupling parameters are kept unchanged for parametrizations of the TM1$\omega\rho$ family with different values of L.

The right panel of the same figure represents the M-R curves of the same models. For $L = 108$ MeV the Λ-hyperon is the responsible for almost all the strangeness content and, therefore, it is not sensitive to the Σ potential. On the other hand, models with smaller values of L are sensitive to the Σ potential and a change of $U_\Sigma(n_0)$ between -10 and $+30$ MeV is translated into a reduction of $\sim 20\%$ of the total strangeness content and an increase of $300 - 400$ m of the star radius. The overall effect on the radius due to the inclusion of hyperons in the family of models considered in this section is a reduction of at most 400 to 600m. Let us recall that several authors, including (Horowitz and Piekarewicz, 2001b; Lattimer and Prakash, 2001; Carriere et al., 2003; Cavagnoli et al., 2011; Lattimer and Steiner, 2014; Pais and Providência, 2016), have shown that the NS radius is correlated with the nucleus neutron skin, a quantity directly related with the slope of the symmetry energy: the larger the slope of the symmetry energy the larger the radius. This behavior is clearly seen in the left panel of **Figure 5**: for the non-hyperonic models, located on the vertical axis where $N_S/N_B = 0$ of the left panel, the radius of a $1.67M_\odot$ increases with the symmetry energy slope L, and a difference in radius of almost 1 km is obtained between models with $L = 56$ MeV and $L = 108$ MeV.
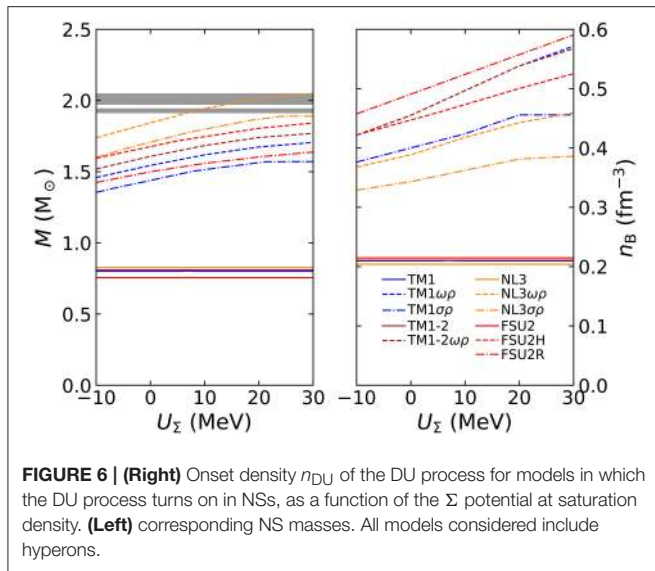
FIGURE 6 | (Right) Onset density n_{DU} of the DU process for models in which the DU process turns on in NSs, as a function of the Σ potential at saturation density. **(Left)** corresponding NS masses. All models considered include hyperons.

5.3. Effect of the Σ Potential

It was shown in the previous section that besides the symmetry energy the value of Σ potential in symmetric matter at saturation, chosen to fix the value of the σ-meson coupling, could also have a strong effect on the properties of the star, in particular, if the model has a small value of L. In the following, we analyse this effect and, taking into account that the Σ-meson interaction is still not constrained, we allow it to vary between -10 and 30 MeV, although, as discussed in section 4, experimental results seem to indicate it is repulsive in nuclear matter.

5.3.1. Direct Urca Process

In this section, we consider the set of models defined in section 2. We have discussed in the previous section the effect of the density dependence of the symmetry energy on the onset of the nucleonic electron DU process, whether hyperons are included and present or not. In **Figure 6** left panel, we plot the DU onset density for the different models as a function of $U_{\Sigma}(n_0)$ the Σ potential in symmetric nuclear matter at saturation. In the right panel, the corresponding NS masses are shown. Models with a large L, i.e., NL3, TM1, and FSU2, are not affected because n_{DU} is just above saturation density and lower than any of the hyperon onset density. For all the other models the trend is similar: the more repulsive $U_{\Sigma}(n_0)$ is, the larger n_{DU}.

To conclude, let us point out that the two models with density dependent couplings do not predict the occurrence of the DU process, even in the presence of hyperons.

5.3.2. Hyperon Species

In section 5.2 we have indicated the different channels that allow for hyperonic direct Urca. It is, therefore, important to determine under which conditions these processes occur, in particular, the masses of the NSs for which they are opened. In the present section we discuss for the models of **Table 1** the maximum mass central density, the onset density of the different hyperons and
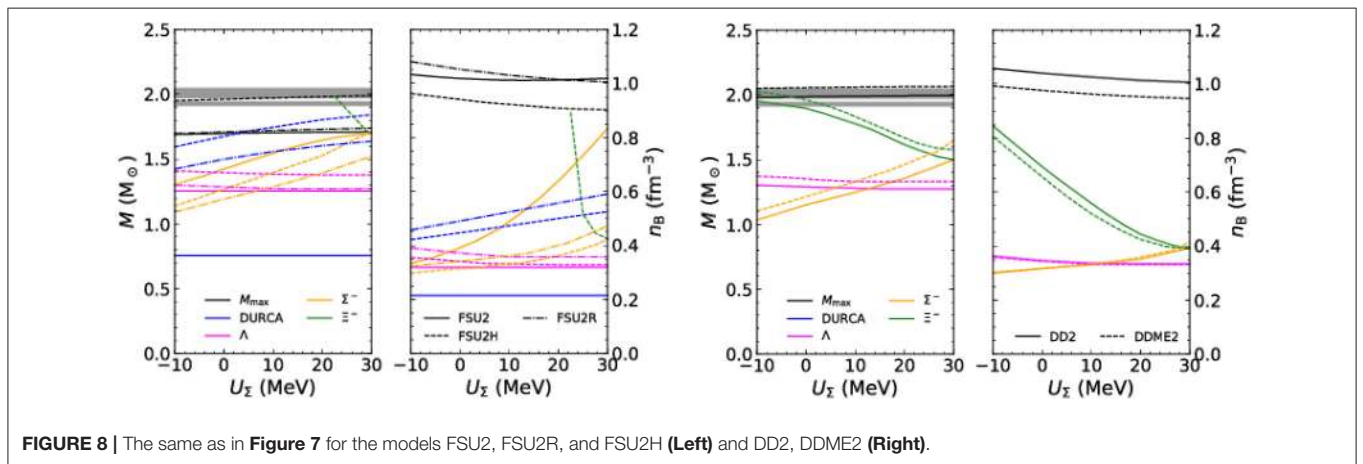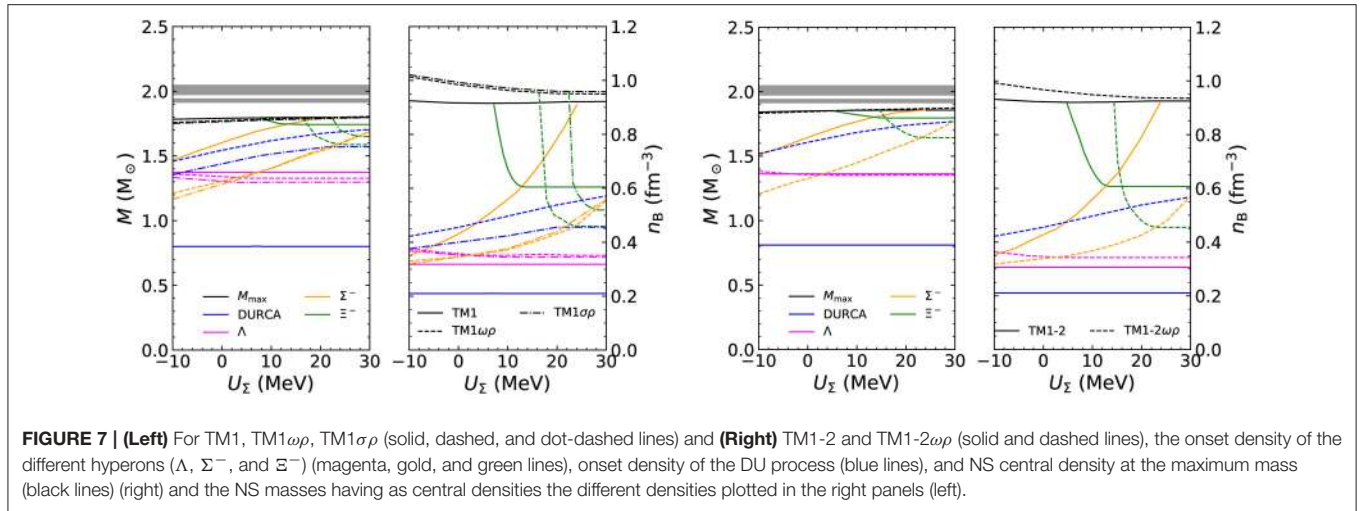
the onset density of the nucleonic electron DU process as a function of the U_{Σ}, and the corresponding NS masses.

In **Figure 7**, the above information is plotted for TM1, TM1$\omega\rho$ and TM1$\sigma\rho$ MeV (left panels), and for TM1-2 and TM1-2$\omega\rho$ (right panels). Models with a non-linear term in $\omega\rho$ or $\sigma\rho$ have $L \simeq 55$ MeV while TM1 and TM1-2 have a slope that is twice as large: $L \sim 110$ MeV. All these models give a maximum mass below $1.9\,M_{\odot}$.

The behavior of the TM1 and TM1-2 EoS only differ above saturation density, the TM1-2 EoS being stiffer. As a consequence, hyperons set in at lower densities in TM1-2, and the maximum masses are larger, but still below $1.9\,M_{\odot}$, for the set of hyperon-meson coupling chosen which considers for the vector-isoscalar mesons the $SU(6)$ symmetry. For TM1 and TM1-2 as discussed before, the DU sets in NSs with masses below $1\,M_{\odot}$, independently of U_{Σ}. Models including the non-linear term $\omega\rho$ or $\sigma\rho$, and having a symmetry energy slope $L \sim 55$ MeV, show a very different behavior. In this case, the magnitude of $U_{\Sigma}(n_0)$ has an important effect on the behavior of the system: for $U_{\Sigma} \lesssim 5$ MeV, the Σ hyperon sets in at densities below the onset of Λ, and the corresponding NS have masses below $\sim 1.2\,M_{\odot}$, that is $\sim 0.2 - 0.3 M_{\odot}$ smaller than the mass of the star where the nucleonic electron DU process starts operating. For $U_{\Sigma} \gtrsim 5$ MeV, the Λ-hyperon is the first hyperon to set in and is not affected by the magnitude of $U_{\Sigma}(n_0)$. This occurs for stars with a mass $\sim 1.3\,M_{\odot}$. If $U_{\Sigma} \gtrsim 20$ MeV, the Ξ^--hyperon sets in before Σ^-, corresponding to a star mass of $\sim 1.6\,M_{\odot}$. It is interesting to comment on the differences between models TM1$\omega\rho$ and TM1$\sigma\rho$ which have the same symmetry energy slope at saturation, but the density dependence of the symmetry energy in TM1$\omega\rho$ is modeled by the coupling of the ω-meson to the ρ-meson, while in TM1$\sigma\rho$ the ρ-meson couples to the σ-meson. Within TM1$\sigma\rho$, the onset of the Λ and Σ-hyperons as well as the nucleonic electron DU process occur in stars with lower masses. This is due to the fact that the softening effect on the symmetry energy, which is always very effective in TM1$\omega\rho$ because the ω-field increases with density, saturates in model TM1$\sigma\rho$ due to the behavior of the σ-meson with density. Finally, we also conclude that the overall effect of the value of $U_{\Sigma}(n_0)$ on the star maximum mass is negligible.

Similar conclusions may be drawn for the models NL3, NL3$\omega\rho$, and NL3$\omega\rho$, the main difference being that in this case much larger star masses are attained, well above $\sim 2\,M_{\odot}$, because these EoSs are harder than the EoS resulting from TM1, TM1-2, and respective families. However, for these models the maximum NS masses correspond to configurations where the effective nucleonic mass becomes zero, as already pointed out in Fortin et al. (2017). For this reason we do not show plots obtained with this family of models.

In **Figure 8** left panel, the behavior of models FSU2, FSU2R, and FSU2H is shown. Model FSU2 has a large symmetry energy slope $L = 113$ MeV, and properties similar to the ones of TM1, presenting, however, smaller star masses at the hyperon onset and smaller maximum star masses. FSU2R and FSU2H have been fitted to a different set of properties and, in particular, to a smaller symmetry energy slope ($L \sim 45$ MeV), and were built to describe a $2M_{\odot}$ star, even in the presence of hyperons

FIGURE 7 | (Left) For TM1, TM1$\omega\rho$, TM1$\sigma\rho$ (solid, dashed, and dot-dashed lines) and (Right) TM1-2 and TM1-2$\omega\rho$ (solid and dashed lines), the onset density of the different hyperon (Λ, Σ^-, and Ξ^-) (magenta, gold, and green lines), onset density of the DU process (blue lines), and NS central density at the maximum mass (black lines) (right) and the NS masses having as central densities the different densities plotted in the right panels (left).

FIGURE 8 | The same as in **Figure 7** for the models FSU2, FSU2R, and FSU2H **(Left)** and DD2, DDME2 **(Right)**.

for FSU2H . FSU2 and FSU2R in fact predict similar maximum masses taking the $SU(6)$ symmetry to fit the vector isoscalar mesons, close to 1.75 $M_\odot$, but for FSU2H the maximum mass goes up to $2M_\odot$. Comparing the FSU2H and FSU2R models, it is clear that because FSU2H is harder, the onset of hyperons occurs at smaller densities, which, however, corresponds to larger star masses. As an example, the onset of Λs occur at $\sim$ 1.3$M_\odot$ for FSU2R and at $\sim$ 1.4$M_\odot$ for FSU2H. Also the nucleonic electron DU process turns on for the FSU2H model for masses $\sim$ 0.2 $M_\odot$ larger, and above 1.5$M_\odot$ whichever values of U_Σ is employed, going up to $\sim$ 1.7$M_\odot$ for $U_\Sigma = +30$ MeV. The Σ-hyperon appears before the Λ-hyperon in these two models at larger values of U_Σ than discussed before, i.e., for $U_\Sigma \lesssim +10$ MeV. For such a slightly attractive potential hyperons appears already in stars with masses below 1.25$M_\odot$. One difference with respect to the previous NL3, TM1 and TM1-2-like models is that for the FSU2 like models, the Ξ-meson does not set in before the Σ-hyperon for $U_\Sigma \leq +30$ MeV. This is a consequence of the large isospin of Σ^- that compensates the repulsion of the Σ potential in symmetric nuclear matter. In order to analyze the effect of the present results on the cooling of the NSs, one would

need to take into account the nucleonic and hyperonic pairing (Raduta et al., 2017; Negreiros et al., 2018), and this will be left for a future work.

We finally consider the two models with density-dependent parameters, see **Figure 8** right panel. They have very similar behaviors, the only difference being that, since the DDME2 EoS is slightly harder, the incompressibility at saturation is $K = 251$ MeV, the onset of hyperons and of the nucleonic DU process occur at smaller densities and slightly larger star masses ($\sim 0.1M_\odot$). Just as for the FSU2-like models, for these two models the Ξ^--hyperon does not set in before the Σ^- for $U_\Sigma(n_0)$ in the range $-10, +30$ MeV. The Λ-meson appears in stars with $M = 1.3 - 1.4M_\odot$ and if $U_\Sigma \sim -10$ MeV stars with $M \sim 1 - 1.1M_\odot$ already contain Σ-hyperons. The two density-dependent models do not allow for the nucleonic electron DU process to turn on. However, the hyperonic DU processes operate inside the stars, and for $U_\Sigma \leq 10$ MeV the process described in Equation (26) is already open for stars with $M \sim 1.3M_\odot$.

Before finishing this section we would like to discuss the effect of the uncertainties introduced in the previous discussion by fixing the U_Ξ in symmetric matter to -18 MeV and by
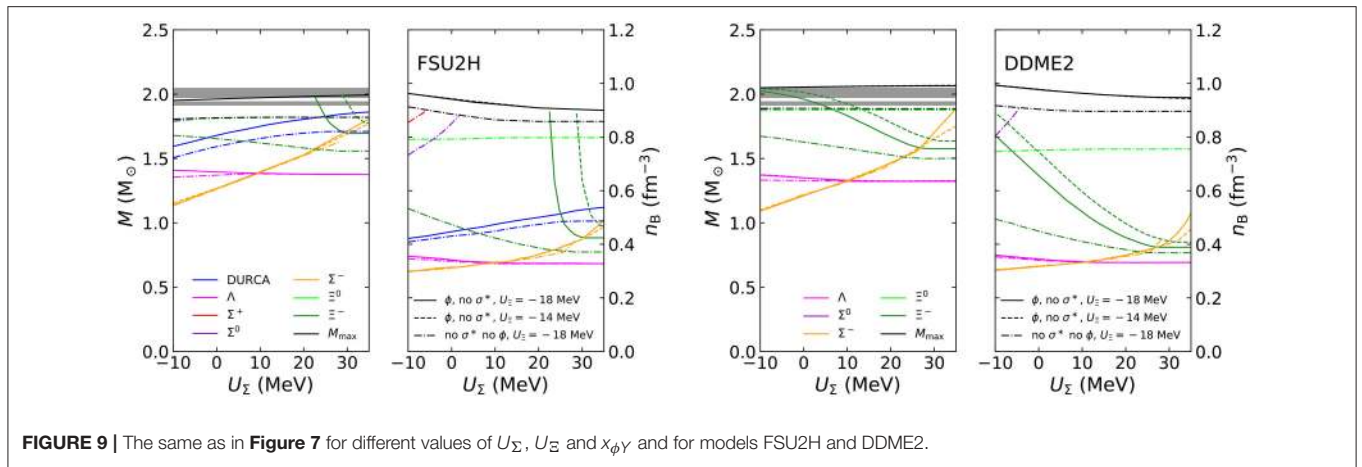
FIGURE 9 | The same as in **Figure 7** for different values of U_Σ, U_Ξ and $x_{\phi Y}$ and for models FSU2H and DDME2.

the unconstrained couplings of the Σ and Ξ-hyperons to the ϕ-meson.

Following (Khaustov et al., 2000), we could have considered $U_\Xi(n_0) = -14$ MeV. In **Figure 9** the solid (dashed) lines were obtained with $U_\Xi = -18(-14)$ MeV. The curves corresponding to these two calculations are generally superposed, except for the ones showing the onset density of the Ξ-hyperon, which will occur at a density 0.05–0.1 fm^{-3} larger, if the higher value of U_Ξ is considered. All other properties, such as the onset of the DU process and of the other hyperons are insensitive to this change of U_Ξ, except if the Σ potential is so repulsive that the Ξ hyperon sets in before the Σ hyperon. If future experiments show that the Σ potential is very repulsive in symmetric nuclear matter, models will be more sensitive to the Ξ hyperon interaction.

We discuss in the following the role of the ϕ meson. In **Figure 9**, for the FSU2H and DDME2 models the result of switching off the coupling of the hyperons Σ and Ξ to the ϕ meson [as in the maximal hyperonic models defining a lower limit on the NS mass (Fortin et al., 2017)] are compared with the previous calculations for which the ϕ couplings to Σ and Ξ hyperons are fixed to the $SU(6)$ values. The ϕ meson is responsible for the description of the YY interaction and, therefore, its effect is noticeable at high densities but not on the first hyperon to appear, for which it is the YN interaction that plays a role. Once the first hyperon sets in, not including the coupling to the ϕ-meson results in an earlier onset (lower density) of the other hyperons. In particular, the Ξ hyperon is strongly affected because, having strangeness -2, the coupling of the ϕ meson to the Ξ hyperon is two times larger. An immediate consequence of this last effect is that the maximum mass configuration is lowered and for both FSU2H and DDME2 it falls below $1.9 M_\odot$, the mass of the PSR J1614$-$2230. Removing the ϕ-meson also affects the DU process in the FSU2H model, bringing its onset to lower densities, because of an increased hyperon content and thus a reduction of the neutron Fermi momentum which ultimately favors the occurrence of the DU process.

5.3.3. Steady Thermal State of Accreting NSs

We now explore how the value of the U_Σ potential and of the symmetry energy affects the cooling of NSs. In particular, we

model the thermal state of NSs in Soft X-ray transients (SXTs) and focus more specifically on SAX J1808.4-3658 (SAX J1808 in the following) (Campana et al., 2002; Heinke et al., 2009), the SXT with the lowest-observed luminosity.

Very recently, three works focused on the study of the cooling of isolated middle-aged neutron stars containing hyperons in their interior (Raduta et al., 2017; Grigorian et al., 2018; Negreiros et al., 2018). The discussion in Raduta et al. (2017) has been performed in the framework of the DDME2 relativistic density functional and including pairing in the hyperonic sector, for the Λ and well as the Σ^- and Ξ^--hyperons, with hyperonic pairing gap equations calculated within the Bardeen-Cooper-Schrieffer approach. It was shown that the hyperons play an important role in the cooling of neutron stars. The authors considered a highly repulsive interaction between Σ^-. In Negreiros et al. (2018) the authors also take a repulsive interaction for the Σ^- and perform cooling simulations having as underlying models FSU2, FSU2R, and FSU2H and including nucleon pairing only. They conclude that cooling observations seem to be more compatible with an a soft symmetry energy EoS. In Grigorian et al. (2018) the authors compute the cooling evolution of NS using a stiff EoS, MKVORHϕ including hyperons (Maslov et al., 2016), and a repulsive Σ^- potential. They include nucleon and Λ pairing and show that their cooling curves are quite sensitive to the proton-proton gap. The present available cooling data are explained within this models by either including or not including hyperons, if appropriate pairing gaps are chosen and one considers that different sources have different masses. In the following we will only consider transiently accreting neutron stars. No pairing effects will be included and, therefore, we should interpret the results obtained as lower limits for the heating curves. In Han and Steiner (2017) and Fortin et al. (2018b), thermal states of neutron stars in soft x-ray transients were studied within nucleonic models and the authors concluded that the interpretation of observational data requires that the direct Urca process has to occur and superfluidity pairing gaps should be small.

In SXTs NSs accrete matter from their binary companion during short phases with a high luminosity followed by long period of quiescence characterized by a low luminosity signaling zero or strongly reduced accretion. During the accretion phases,
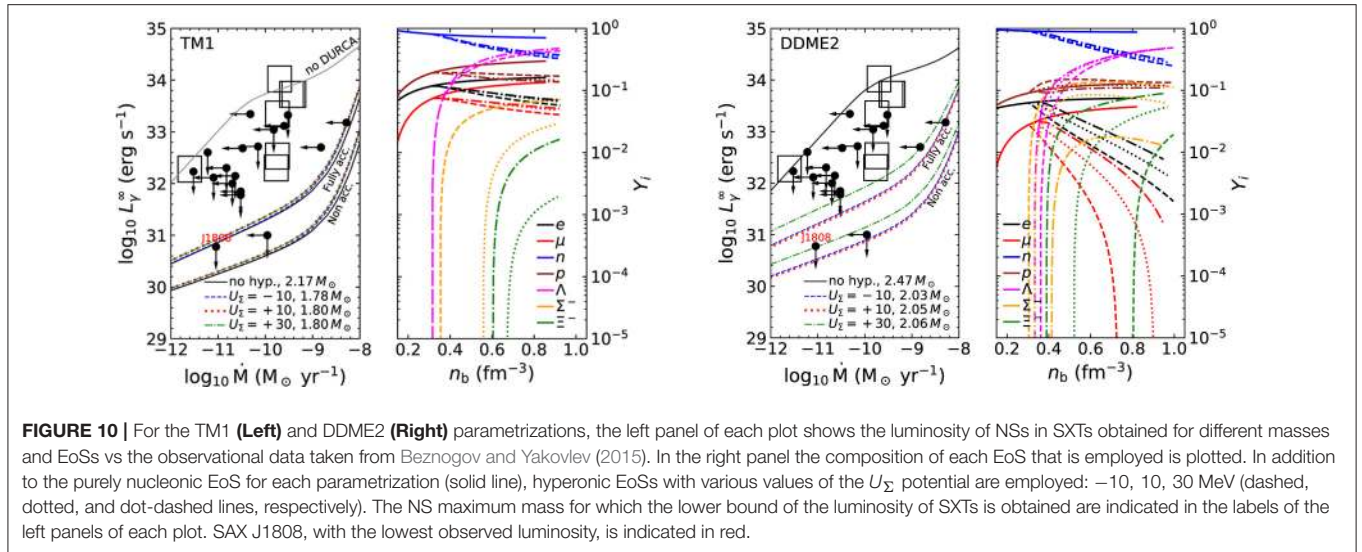
the accreted matter undergoes a series of nuclear reactions [electron captures and pycnonuclear fusions—see (Haensel and Zdunik, 2008) and references therein] as it sinks deeper into the crust under the weight of the newly-accreted matter. These reactions release heat in the crust which propagates in the NS interior, inwards heating the core and outwards emitted in the form of photons at the surface. This is the so-called deep crustal heating. After frequent and short periods of accretion the NS reaches a state of thermal equilibrium with a constant internal temperature throughout the star (Yakovlev and Pethick, 2004; Yakovlev et al., 2004). This temperature is determined by the balance between the heating generated during the accretion phase, which is directly proportional to the accretion rate $\dot{M}$ averaged over periods of accretion and quiescence, and the energy losses in the form of (1) photons emitted from the surface of the star and (2) of neutrinos freely escaping from the whole star (see e.g., Fortin et al., 2018b for details). Consequently the steady thermal states of accreting NS depends on three ingredients (1) the composition of the NS envelope from where the photons escape; (2) the NS core properties (EoS and composition) since the core is responsible for most of the neutrino losses; (3) the total heat release in the accreted crust. The EoS for the crust hardly affects the thermal states, only the heat release per accreted nucleon Q_{DCH} does and its values have been shown to be rather robust: $Q_{DCH} \sim 2$ MeV per accreted nucleon (Haensel and Zdunik, 2008; Fantina et al., 2018). Thus, in the following we adopt the model for the accreted crust and the deep crustal heating from Haensel and Zdunik (2008) for lack of model consistent with the core EoSs that we employ. We use two limiting models of NS envelopes corresponding to either the absence of light elements (non-accreted envelope) or a maximum amount of them (fully accreted envelope) from Potekhin et al. (2003).

In **Figure 10** for the TM1 (left) and DDME2 (right) EoSs, we show, on the left panel of each plot the luminosity in quiescence as a function of the accretion rate together with the observational data from (Beznogov and Yakovlev, 2015) and on the right panel the composition for the different models. We use the TM1 and DDME2 EoSs with various hyperonic contents obtained for different values of the Σ potential (dashed, dotted, and dot-dashed lines) together with their purely nucleonic versions (solid lines). TM1 is chosen as a representative model that predicts that the nucleonic DU process occurs for quite low star masses $M < 0.8 M_\odot$ while DDME2 as a model which does not allow for this process at all. For each EoS we compute (1) the upper bound on the thermal state of NSs that is obtained for NSs with a mass below the DU threshold—this defines the lowest possible neutrino losses and hence the largest luminosity, (2) the lower bound of the thermal state which is reached for maximum mass NSs with the largest neutrino emissions obtained when the DU processes operate and hence the lowest luminosity. We do not include superfluidity in the models (see discussion in Fortin et al., 2018b) as it reduces the DU emissivity. We indeed want to confront the lowest-bound on the thermal state we obtain with the observational data on SAX J1808. This object, indicated in red in the plots in **Figure 10**, has the lowest observed luminosity and a precisely measured accretion rate thanks to the

observations of multiple type I X-ray bursts (Heinke et al., 2009). Its low-luminosity is challenging to model and suggests that very efficient neutrino processes, the most efficient of which are the nucleonic and hyperonic DU processes, are operating in its NS core. In Yakovlev and Pethick (2004), the authors could explain its luminosity only by using an hyperonic core EoS. The model they have considered for nuclear matter is GL85 (Glendenning, 1985) that predicts a quite hard EoS with an incompressibility $K = 285$ MeV and a symmetry energy at saturation $E_{sym} = 36.8$ MeV. For the hyperonic interaction the universal couplings were considered, i.e., the hyperon-meson couplings equal the nucleon-meson couplings. This choice gives rise to strongly attractive hyperon potentials in symmetric nuclear matter at saturation, of the order -60 to -70 MeV, and allows for the appearance of all six hyperons inside the maximum mass star, and, therefore, all channels defined by Equations (24–31) are opened. As a consequence in addition to the nucleonic DU process all hyperonic processes are turned on and hence the neutrino emissivity is larger and the luminosity lower for the hyperonic EoS than for purely nucleonic one. The low-luminosity of SAX J1808 could only then be modeled for a hyperonic NS, suggesting that hyperons could be present in SAX J1808.

For the hyperonic TM1 EoSs on the left plot in **Figure 10**, in addition to the nucleonic DU process, for the model with a slightly attractive potential, $U_\Sigma = -10$ MeV the DU channels in Equations (26, 28, 31) are operating in the star with the maximum mass, for a repulsive $U_\Sigma = 10$ MeV the DU process in Equation (30) is turned on as the Ξ^- is present. However, since the Σ^- appears at larger densities than when an attractive potential is used, the most efficient of all hyperonic DU processes turned on for such models, is the one in Equation (26) that then operates in a smaller region of the star and the process in Equation (30) is too weak to compensate these lesser neutrinos losses. For the model with $U_\Sigma = 30$ MeV since no Σ^- are present only processes in Equations (28) and (30) set in and both are less efficient than the one in Equation (30). Hence the model with the $U_\Sigma = -10$ MeV is the coolest of all hyperonic models. We obtain that the purely nucleonic has the lowest luminosity compared to hyperonic models but the difference is quite small. The purely nucleonic NS, in which only the nucleonic DU process, which is the most efficient process, operates is almost $\sim 0.2 M_\odot$ more massive than the hyperonic NSs. Hence for hyperonic NSs even if more DU channels are opened, these are less efficient and do not exactly compensate for the fact that the nucleonic NS has an extra region of $0.2 M_\odot$ emitting neutrinos via the most efficient channel. Thus, hyperonic stars emit all in all less neutrinos and hence have a slightly larger luminosity. As in Fortin et al. (2018b) we obtain that NSs with a fully accreted envelope are more luminous than with a non-accreted one. Thus, we obtain that for the TM1 EoS SAX J1808 is compatible with a NS with a small or null amount of accreted matter in the envelope, with or without hyperons.

For the DD2 parametrization (right plots of **Figure 10**), as the nucleonic DU process does not operate at all for the purely nucleonic EoS, non-hyperonic NSs will have a very similar and large luminosity. Hyperonic models have, however, a small luminosity as the additional hyperonic DU processes operates and only such models can explain the low-luminosity of SAX

FIGURE 10 | For the TM1 **(Left)** and DDME2 **(Right)** parametrizations, the left panel of each plot shows the luminosity of NSs in SXTs obtained for different masses and EoSs vs the observational data taken from Beznogov and Yakovlev (2015). In the right panel the composition of each EoS that is employed is plotted. In addition to the purely nucleonic EoS for each parametrization (solid line), hyperonic EoSs with various values of the U_Σ potential are employed: −10, 10, 30 MeV (dashed, dotted, and dot-dashed lines, respectively). The NS maximum mass for which the lower bound of the luminosity of SXTs is obtained are indicated in the labels of the left panels of each plot. SAX J1808, with the lowest observed luminosity, is indicated in red.

J1808. For all hyperonic models the Ξ^-, Σ^-, and Λ are present at the maximum mass, and the latter two species in similar amount. The most efficient hyperonic DU process is then the channel in Equation (26) between the Λ and the Σ^-. As the model with $U_\Sigma = -10$ MeV has the largest amount of Σ^- (it even appears before the Λ) it has the largest neutrino emissivity and hence the lowest luminosity of all models. The model with $U_\Sigma = 10$ MeV has approximately 50 % less of Σ^- and hence is slightly more luminous as it emits less neutrinos. Finally for $U_\Sigma = 30$ MeV the fraction of Σ^- is one order of magnitude less than for the slightly attractive potential. As a consequence this model gives the largest luminosity of all hyperonic models. We conclude that for the DDME2 model, since the nucleonic DU process does not operate, SAX J1808 is only compatible with a NS with hyperons and no or a very small amount of accreted matter in the envelope.

We can see that the delicate interplay between the symmetry energy and the Σ-potential strongly affects the cooling of SXTs. These objects could potentially offer the possibility to constraint the Σ-potential and thus the properties of the Σ hyperon, from the astrophysical observations of SXTs with a low-luminosity complementing the little experimental constraints on the properties of the Σ hyperon currently available. A more systematic study of the thermal state of accreting NSs is beyond the scope of the present paper and will be the subject of a future work.
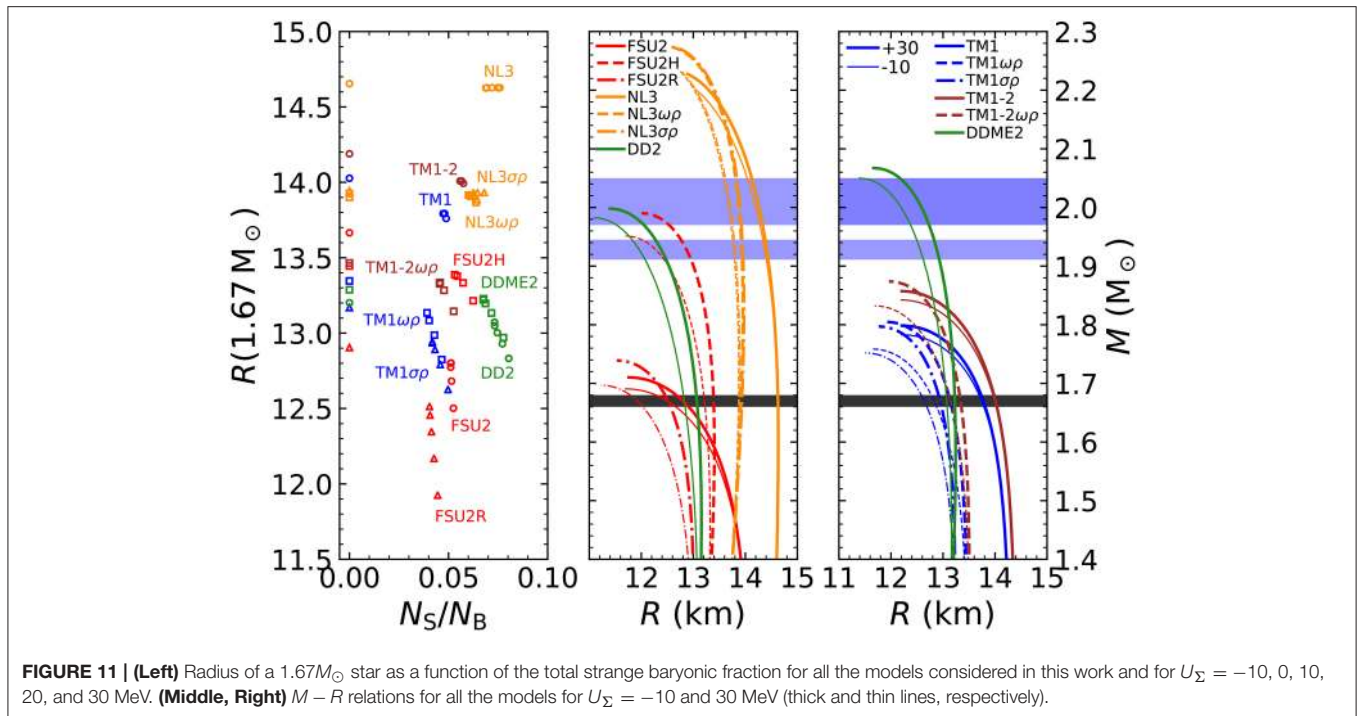
5.3.4. Hyperonic Star Radius

There are still large observational uncertainties associated with the radius of NSs including the canonical NS with a mass equal to $1.4M_\odot$, see the discussion in Potekhin (2014),Fortin et al. (2016a), and Steiner et al. (2016), although there have been several indirect predictions from different analysis. Recently several studies have used the detection of the gravitational waves emitted from a neutron star merger GW170817 (Abbott et al., 2017) to constrain the upper limit of the $1.4M_\odot$ star radius to ~ 13.7 km (Abbott et al., 2018; Annala et al., 2018; Fattoyev et al., 2018; Lim and Holt, 2018; Malik et al., 2018; Most et al.,

2018; Raithel et al., 2018; Tews et al., 2018). Similar constraints had been obtained before from the analysis of the experimental constraints set on the symmetry energy (Li and Steiner, 2006; Steiner et al., 2016).

Since we are interested in analyzing the effect of strangeness on the radius of a NS, and as we have seen for many models, strangeness sets in inside stars with a mass above $1.4M_\odot$, we will again consider a more massive star. In the discussion of this section we calculate the radius of a star with $M = 1.67M_\odot$ as in section. Results are plotted in **Figure 11** left panel as a function of the total star strange baryonic fraction. On the right panel, we have plotted the hyperonic star mass-radius curves to help the discussion. The thin (thick) lines correspond to $U_\Sigma = -10 \,(+30)$ MeV.

The strange baryonic fraction increases if the Σ potential becomes less repulsive, and simultaneously the radius decreases. The relation between the radius and the strange baryonic fraction is essentially linear but the slope is model dependent. For models like NL3, TM1, TM1-2 changing U_Σ does not have a large effect on the strangeness content and on the radius. This is clearly understood looking at **Figure 7** where the star mass at the onset of the Σ hyperon is plotted: a star with $M = 1.67M_\odot$ has no (only a few) Σ hyperons for $U_\Sigma = +30 \,(-10)$ MeV. Density-dependent models have a similar behavior, being the models that predict a larger amount of strangeness, as large as 0.075, although still satisfying the $2M_\odot$ constraint. For $-10 < U_\Sigma < +30$ MeV the radius increases ∼ 300 m. Models TM1$\omega\rho$, TM1$\sigma\rho$, TM1-2$\omega\rho$, FSU2H have a similar behavior but do not predict strangeness contents above 0.05. Models FSU2 and FSU2R suffer a quite large radius change for a small increase of strangeness because, as seen in the right panel, $1.67M_\odot$ is very close to the maximum star mass. Contrary to Providencia and Rabhi (2013) we do not see a linear correlation if also the $N_S/N_B = 0$ radius is included. In Providencia and Rabhi (2013) N_S/N_B is the strangeness fraction defined as the total strangeness number over the total baryonic number and not the strange baryonic fraction. However, in that work the authors did not use unified crust-core

FIGURE 11 | (Left) Radius of a $1.67M_\odot$ star as a function of the total strange baryonic fraction for all the models considered in this work and for $U_\Sigma = -10$, 0, 10, 20, and 30 MeV. **(Middle, Right)** $M - R$ relations for all the models for $U_\Sigma = -10$ and 30 MeV (thick and thin lines, respectively).

EoS and different hyperon interactions, giving rise to much larger strangeness fractions inside the star, were discussed.

6. SUMMARY AND CONCLUSIONS

In the present study, we have explored how the density dependence of the symmetry energy may affect the properties of hyperonic neutron stars. The study was undertaken within the RMF approach to nuclear matter and models that describe ground-state properties of nuclei and Λ-hypernuclei, as well as constraints from microscopic calculations of NS (except for three models) and the $2M_\odot$ constraint on nucleonic stars have been chosen. We have also considered a family of models based on TM1 (Sugahara and Toki, 1994; Providencia and Rabhi, 2013; Bao and Shen, 2014) that has allowed us to directly discuss the effect of the density dependence of the symmetry energy on the properties of hyperonic stars. For all the models considered, we have taken an inner crust-core unified EoS. In the present work, we have calculated the FSU2, FSUR2H, and FSU2H inner crust of catalyzed β-equilibrium matter, which are given as **Table 5**.

The Λ-meson and Ξ-meson couplings were constrained by the existing hypernuclei experimental data. Taking into account the present lack of knowledge concerning the properties of the Σ hyperon in nuclear matter, we have discussed the properties of hyperonic matter considering values of the Σ potential in symmetric nuclear matter that go from -10 MeV to $+30$ MeV at saturation density, having in mind that if no Σ-hypernucleus has been detected, the Σ potential must be repulsive or only slightly attractive.

We have shown that the DU process is affected by hyperons only if the slope of the symmetry energy is $L \lesssim 70$ MeV. The nucleonic electron DU process is both sensitive to the

slope of the symmetry energy and, for $L \lesssim 70$ MeV, to the value of the Σ potential in nuclear matter. The more repulsive U_Σ the larger the nucleonic electron DU process. A small L shifts the DU onset to larger densities but the effect is stronger the more repulsive the Σ potential is. Models with density-dependent couplings simply do not allow for the nucleonic electron DU process to turn on. However, the cooling of stars within this framework is also affected when new hyperonic channels open inside the star. So, even though the density-dependent models do not predict nucleonic electron DU, when the reactions described in Equations (28, 26, 31) start to operate the star is much less luminous. This occurs in stars with a mass of the order of $1.1 - 1.3M_\odot$ models. All other models, with constant couplings, predict the occurrence of both hyperonic and nucleonic DU processes inside massive enough NSs.

We have studied how the value of the U_Σ potential affects the thermal state of NSs in Soft X-ray transients and focused more specifically on SAX J1808 (Campana et al., 2002; Heinke et al., 2009), the SXT with the lowest-observed luminosity. We have shown that the low luminosity of this object could be described by a model, with an unrealistically high symmetry energy slope, that predicts the opening of the DU inside low mass stars, independently of taking a nucleonic or an hyperonic EoS. For the nucleonic EoS, the maximum star mass is large and allows the nucleonic DU process to occur in a wide range of the NS interior, while for the hyperonic EoS although the maximum mass is smaller, inside the core both the nucleonic DU and the hyperonic DU processes act. However, the SAX J1808 low luminosity could also be explained in the framework of a density dependent hadronic model, satisfying well-established nuclear matter and nuclei properties and describing a $2M_\odot$ star, if

hyperonic degrees of freedom are allowed to occur inside the star. In this case, objects like the SAX J1808 could potentially offer the possibility to constraint the hyperonic interaction, in particular, the Σ potential.

DATA AVAILABILITY

All datasets generated for this study are included in the manuscript.

AUTHOR CONTRIBUTIONS

The conception and design of the study was proposed by CP. All authors developed codes for this study. MF produced the figures. CP wrote the first draft of the manuscript. HP and MF wrote sections of the manuscript. All authors contributed to the manuscript revision, read, and approved the submitted version.

FUNDING

REFERENCES

Abbott, B. P., Abbott, R., Abbott, T. D., Acernese, F., Ackley, K., Adams, C., Adams T. (2017). GW170817: observation of gravitational waves from a binary neutron star inspiral. *Phys. Rev. Lett.* 119:161101. doi: 10.1103/PhysRevLett.119.161101

Abbott, B. P., et al. Abbott, B. P., Abbott, R., Abbott, T. D., Acernese, F., Ackley, K., Adams, C., Adams, T. (2018). GW170817: measurements of neutron star radii and equation of state. *Phys. Rev. Lett.* 121:161101. doi: 10.1103/PhysRevLett.121.161101

Abrahamyan, S., Ahmed, Z., Albataineh, H., Aniol, K., Armstrong, D. S., Armstrong, W., et al. (2012). Measurement of the neutron radius of ^{208}Pb through parity violation in electron scattering. *Phys. Rev. Lett.* 108:112502. doi: 10.1103/PhysRevLett.108.112502

Alford, M., Blaschke, D., Drago, A., Klahn, T., Pagliara, G., and Schaffner-Bielich, J. (2007). Quark matter in compact stars? *Nature* 445, E7–E8. doi: 10.1038/nature05582

Alford, M. G., Han, S., and Prakash, M. (2013). Generic conditions for stable hybrid stars. *Phys. Rev.* D88:083013. doi: 10.1103/PhysRevD.88.083013

Alford, M. G., and Sedrakian, A. (2017). Compact stars with sequential QCD phase transitions. *Phys. Rev. Lett.* 119:161104. doi: 10.1103/PhysRevLett.119.161104

Annala, E., Gorda, T., Kurkela, A., and Vuorinen, A. (2018). Gravitational-wave constraints on the neutron-star-matter equation of state. *Phys. Rev. Lett.* 120:172703. doi: 10.1103/PhysRevLett.120.172703

Antoniadis, J., Freire, P. C. C., Wex, N., Tauris, T. M., Lynch, R. S. van Kerkwijk, M. H., et al. (2013). A massive pulsar in a compact relativistic binary. *Science* 340:6131. doi: 10.1126/science.1233232

Arzoumanian, Z., Brazier, A., Burke-Spolaor, S., Chamberlin, S., Chatterjee, S., Christy, B., et al. (2018). The NANOGrav 11-year data set: high-precision timing of 45 millisecond pulsars. *Astrophys. J. Suppl.* 235:37. doi: 10.3847/1538-4365/aab5b0

Avancini, S. S., Marinelli, J. R., Menezes, D. P., de Moraes, M. M. W., and Providencia, C. (2007). Density dependent hadronic models and the relation between neutron stars and neutron skin thickness. *Phys. Rev.* C75:055805. doi: 10.1103/PhysRevC.75.055805

Avancini, S. S., Menezes, D. P., Alloy, M. D., Marinelli, J. R., Moraes, M. M. W., and Providência, C. (2008). Warm and cold pasta phase in relativistic mean field theory. *Phys. Rev.* C 78:015802. doi: 10.1103/PhysRevC.78.015802

Bao, S. S., and Shen, H. (2014). Influence of the symmetry energy on nuclear "pasta" in neutron star crusts. *Phys. Rev.* C89:045807. doi: 10.1103/PhysRevC.89.045807

Baran, V., Colonna, M., Greco, V., and Di Toro, M. (2005). Reaction dynamics with exotic beams. *Phys. Rept.* 410, 335–466. doi: 10.1016/j.physrep.2004.12.004

Baym, G., Pethick, C., and Sutherland, P. (1971). The ground state of matter at high densities: equation of state and stellar models. *Astrophys. J.* 170:299.

Beznogov, M. V., and Yakovlev, D. G. (2015). Statistical theory of thermal evolution of neutron stars. *Mon. Not. R. Astron. Soc.* 447, 1598–1609. doi: 10.1093/mnras/stu2506

Bonanno, L., and Sedrakian, A. (2012). Composition and stability of hybrid stars with hyperons and quark color-superconductivity. *Astron. Astrophys.* 539:A16. doi: 10.1051/0004-6361/201117832

Campana, S., Stella, L., Gastaldello, F., Mereghetti, S., Colpi, M., Israel, G. L., et al. (2002). An xmm-newton study of the 401 hz accreting pulsar sax j1808.4–3658 in quiescence. *Astrophys. J. Lett.* 575:L15. doi: 10.1086/342505

Carbone, A., Colò, G., Bracco, A., Cao, L.-G., Bortignon, P. F., Camera, F., et al. (2010). Constraints on the symmetry energy and neutron skins from pygmy resonances in ^{68}Ni and ^{132}Sn. *Phys. Rev. C* 81:041301. doi: 10.1103/PhysRevC.81.041301

Carriere, J., Horowitz, C. J., and Piekarewicz, J. (2003). Low mass neutron stars and the equation of state of dense matter. *Astrophys. J.* 593, 463–471. doi: 10.1086/376515

Cavagnoli, R., Menezes, D. P., and Providencia, C. (2011). Neutron star properties and the symmetry energy. *Phys. Rev.* C84:065810. doi: 10.1103/PhysRevC.84.065810

Centelles, M., Roca-Maza, X., Viñas, X., and Warda, M. (2009). Nuclear symmetry energy probed by neutron skin thickness of nuclei. *Phys. Rev. Lett.* 102:122502. doi: 10.1103/PhysRevLett.102.122502

Chatterjee, D., and Vidaña, I. (2016). Do hyperons exist in the interior of neutron stars? *Eur. Phys. J.* A52:29. doi: 10.1140/epja/i2016-16029-x

Chen, W.-C., and Piekarewicz, J. (2014). Building relativistic mean field models for finite nuclei and neutron stars. *Phys. Rev.* C90:044305. doi: 10.1103/PhysRevC.90.044305

Colucci, G., and Sedrakian, A. (2013). Equation of state of hypernuclear matter: Impact of hyperon-scalar-meson couplings. *Phys. Rev. C* 87:055806. doi: 10.1103/PhysRevC.87.055806

Cozma, M. D. (2018). Feasibility of constraining the curvature parameter of the symmetry energy using elliptic flow data. *Eur. Phys. J. A* 54:40. doi: 10.1140/epja/i2018-12470-1

Demorest, P., Pennucci, T., Ransom, S., Roberts, M., and Hessels, J. (2010). Shapiro delay measurement of a two solar mass neutron star. *Nature* 467, 1081–1083. doi: 10.1038/nature09466

Drago, A., Lavagno, A., Pagliara, G., and Pigato, D. (2016). The scenario of two families of compact stars. *Eur. Phys. J.* A52:40. doi: 10.1140/epja/i2016-16040-3

Ducoin, C., Margueron, J., Providencia, C., and Vidana, I. (2011). Core-crust transition in neutron stars: predictivity of density developments. *Phys. Rev.* C83:045810. doi: 10.1103/PhysRevC.83.045810

Dutra, M., Lourenço, O., Avancini, S., Carlson, B., Delfino, A., Menezes, D. P., et al. (2014). Relativistic mean-field hadronic models under nuclear matter constraints. *Phys. Rev.* C90:055203. doi: 10.1103/PhysRevC.90.055203

Fantina, A. F., Zdunik, J. L., Chamel, N., Pearson, J. M., Haensel, P., and Goriely, S. (2018). Crustal heating in accreting neutron stars from the nuclear energy-density functional theory. I. Proton shell effects and neutron-matter constraint. *Astron. Astrophys.* 620:A105. doi: 10.1051/0004-6361/201833605

Fattoyev, F. J., Newton, W. G., and Li, B.-A. (2014). Quantifying correlations between isovector observables and the density dependence of the nuclear symmetry energy away from saturation density. *Phys. Rev. C* 90:022801. doi: 10.1103/PhysRevC.90.022801

Fattoyev, F. J., and Piekarewicz, J. (2013). Has a thick neutron skin in ^{208}Pb been ruled out? *Phys. Rev. Lett.* 111:162501. doi: 10.1103/PhysRevLett.111.162501

Fattoyev, F. J., Piekarewicz, J., and Horowitz, C. J. (2018). Neutron skins and neutron stars in the multimessenger era. *Phys. Rev. Lett.* 120:172702. doi: 10.1103/PhysRevLett.120.172702

Fortin, M., Avancini, S. S., Providência, C., and Vidaña, I. (2017). Hypernuclei and massive neutron stars. *Phys. Rev. C* 95:065803. doi: 10.1103/PhysRevC.95.065803

Fortin, M., Bejger, M., Haensel, P., and Zdunik, J. L. (2016a). Progenitor neutron stars of the lightest and heaviest millisecond pulsars. *Astron. Astrophys.* 586:A109. doi: 10.1051/0004-6361/201424911

Fortin, M., Oertel, M., and Providência, C. (2018a). Hyperons in hot dense matter: what do the constraints tell us for equation of state? *Publ. Astron. Soc. Austral.* 35:44. doi: 10.1017/pasa.2018.32

Fortin, M., Providência, C., Raduta, A. R., Gulminelli, F., Zdunik, J. L., Haensel, P., et al. (2016b). Neutron star radii and crusts: uncertainties and unified equations of state. *Phys. Rev.* C94:035804. doi: 10.1103/PhysRevC.94.035804

Fortin, M., Taranto, G., Burgio, G. F., Haensel, P., Schulze, H. J., and Zdunik, J. L. (2018b). Thermal states of neutron stars with a consistent model of interior. *Mon. Not. R. Astron. Soc.* 475, 5010–5022. doi: 10.1093/mnras/sty147

Freire, P., Bassa, C., Wex, N., Stairs, I., Champion, D., Ransom, S., et al. (2011). On the nature and evolution of the unique binary pulsar j1903+ 0327. *Mon. Not. R. Astron. Soc.* 412, 2763–2780. doi: 10.1111/j.1365-2966.2010.18109.x

Fukushima, K., and Kojo, T. (2016). The Quarkyonic Star. *Astrophys. J.* 817:180. doi: 10.3847/0004-637X/817/2/180

Gal, A. (2010). Strangeness nuclear physics - 2010: overview of strangeness nuclear physics. *Prog. Theor. Phys. Suppl.* 186, 270–281. doi: 10.1143/PTPS.186.270

Gal, A., Hungerford, E. V., and Millener, D. J. (2016). Strangeness in nuclear physics. *Rev. Mod. Phys.* 88:035004. doi: 10.1103/RevModPhys.88.035004

Gandolfi, S., Carlson, J., and Reddy, S. (2012). The maximum mass and radius of neutron stars and the nuclear symmetry energy. *Phys. Rev.* C85:032801. doi: 10.1103/PhysRevC.85.032801

Glendenning, N. K. (1985). Neutron stars are giant hypernuclei? *Astrophys. J.* 293, 470–493. doi: 10.1086/163253

Glendenning, N. K., and Moszkowski, S. A. (1991). Reconciliation of neutron star masses and binding of the lambda in hypernuclei. *Phys. Rev. Lett.* 67, 2414–2417. doi: 10.1103/PhysRevLett.67.2414

Grigorian, H., Voskresensky, D. N., and Maslov, K. A. (2018). Cooling of neutron stars in "nuclear medium cooling scenario" with stiff equation of state including hyperons. *Nucl. Phys.* A980, 105–130. doi: 10.1016/j.nuclphysa.2018.10.014

Grill, F., Pais, H., Providência, C., Vidaña, I., and Avancini, S. S. (2014). Equation of state and thickness of the inner crust of neutron stars. *Phys. Rev.* C90:045803. doi: 10.1103/PhysRevC.90.045803

Grill, F., Providencia, C., and Avancini, S. S. (2012). The Neutron star inner crust and symmetry energy. *Phys. Rev.* C85:055808. doi: 10.1103/PhysRevC.85.055808

Haensel, P., and Pichon, B. (1994). Experimental nuclear masses and the ground state of cold dense matter. *Astron. Astrophys.* 283:313.

Haensel, P., and Zdunik, J. L. (2008). Models of crustal heating in accreting neutron stars. *Astron. Astrophys.* 480, 459–464. doi: 10.1051/0004-6361/200 78578

Haidenbauer, J., and Meißner, U.-G. (2015). A study of hyperons in nuclear matter based on chiral effective field theory. *Nucl. Phys. A* 936, 29–44. doi: 10.1016/j.nuclphysa.2015.01.005

Han, S., and Steiner, A. W. (2017). Cooling of neutron stars in soft x-ray transients. *Phys. Rev.* C 96:035802. doi: 10.1103/PhysRevC.96.035802

Harada, T., Honda, R., and Hirabayashi, Y. (2018). Repulsion and absorption of the Σ-nucleus potential for $\Sigma^- - ^5$He in the ^{6}Li(π^-, K^+) reaction. *Phys. Rev. C* 97:024601. doi: 10.1103/PhysRevC.97.024601

Hebeler, K., Lattimer, J. M., Pethick, C. J., and Schwenk, A. (2013). Equation of state and neutron star properties constrained by nuclear physics and observation. *Astrophys. J.* 773:11. doi: 10.1088/0004-637X/773/1/11

Heinke, C. O., Jonker, P. G., Wijnands, R., Deloye, C. J., and Taam, R. E. (2009). Further constraints on thermal quiescent X-Ray emission from SAX J1808.4-3658. *Astrophys. J.* 691, 1035–1041. doi: 10.1088/0004-637X/691/2/1035

Honda, R., Agnello, M., Ahn, J. K., Ajimura, S., Akazawa, Y., Amano, N., et al. (2017). Missing-mass spectroscopy with the ^{6}Li(π^-, K^+)x reaction to search for $^6_\Lambda$H. *Phys. Rev. C* 96:014005. doi: 10.1103/PhysRevC.96.014005

Horowitz, C. J., and Piekarewicz, J. (2001a). Neutron star structure and the neutron radius of Pb-208. *Phys. Rev. Lett.* 86:5647. doi: 10.1103/PhysRevLett.86.5647

Horowitz, C. J., and Piekarewicz, J. (2001b). The Neutron radii of Pb-208 and neutron stars. *Phys. Rev.* C64:062802. doi: 10.1103/PhysRevC.64.062802

Horowitz, C. J., and Piekarewicz, J. (2002). Constraining urca cooling of neutron stars from the neutron radius of ^{208}Pb. *Phys. Rev. C* 66:055803. doi: 10.1103/PhysRevC.66.055803

Khaustov, P., et al. Khaustov, P., Alburger, D. E., Barnes, P. D., Bassalleck, B., Berdoz, A. R., Biglan, A. (2000). Evidence of Xi hypernuclear production in the C-12(K-,K+)(Xi)Be-12 reaction. *Phys. Rev.* C61:054603. doi: 10.1103/PhysRevC.61.054603

Klähn, T., Łastowiecki, R., and Blaschke, D. B. (2013). Implications of the measurement of pulsars with two solar masses for quark matter in compact stars and heavy-ion collisions: a Nambu-Jona-Lasinio model case study. *Phys. Rev.* D88:085001. doi: 10.1103/PhysRevD.88.085001

Klahn, T., et al. Klähn, T., Blaschke, D., Typel, S., van Dalen, E. N. E., Faessler, A., Fuchs, C. (2006). Constraints on the high-density nuclear equation of state from the phenomenology of compact stars and heavy-ion collisions. *Phys. Rev.*, C74:035802. doi: 10.1103/PhysRevC.74.035802

Klimkiewicz, A., Paar, N., Adrich, P., Fallot, M., Boretzky, K., Aumann, T., et al. (2007). Nuclear symmetry energy and neutron skins derived from pygmy dipole resonances. *Phys. Rev. C* 76:051603. doi: 10.1103/PhysRevC.76.051603

Lalazissis, G. A., Konig, J., and Ring, P. (1997). A new parametrization for the Lagrangian density of relativistic mean field theory. *Phys. Rev.* C55:540–543. doi: 10.1103/PhysRevC.55.540

Lalazissis, G. A., Nikšić, T., Vretenar, D., and Ring, P. (2005). New relativistic mean-field interaction with density-dependent meson-nucleon couplings. *Phys. Rev. C* 71:024312. doi: 10.1103/PhysRevC.71.024312

Lattimer, J. M., and Lim, Y. (2013). Constraining the Symmetry Parameters of the Nuclear Interaction. *Astrophys. J.* 771:51. doi: 10.1088/0004-637X/771/1/51

Lattimer, J. M., Pethick, C. J., Prakash, M., and Haensel, P. (1991). Direct URCA process in neutron stars. *Phys. Rev. Lett.* 66, 2701–2704. doi: 10.1103/PhysRevLett.66.2701

Lattimer, J. M., and Prakash, M. (2001). Neutron star structure and the equation of state. *Astrophys. J.* 550:426. doi: 10.1086/319702

Lattimer, J. M., and Steiner, A. W. (2014). Constraints on the symmetry energy using the mass-radius relation of neutron stars. *Eur. Phys. J. A*50:40. doi: 10.1140/epja/i2014-14040-y

Li, B.-A., Chen, L.-W., and Ko, C. M. (2008). Recent progress and new challenges in isospin physics with heavy-ion reactions. *Phys. Rept.* 464, 113–281. doi: 10.1016/j.physrep.2008.04.005

Li, B.-A., Ramos, A., Verde, G., and Vidana, I. (2014). Topical issue on nuclear symmetry energy. *Eur. Phys. J. A*50:9. doi: 10.1140/epja/i2014-14009-x

Li, B.-A., and Steiner, A. W. (2006). Constraining the radii of neutron stars with terrestrial nuclear laboratory data. *Phys. Lett.* B642, 436–440. doi: 10.1016/j.physletb.2006.09.065

Lim, Y., and Holt, J. W. (2018). Neutron star tidal deformabilities constrained by nuclear theory and experiment. *Phys. Rev. Lett.* 121:062701. doi: 10.1103/PhysRevLett.121.062701

Logoteta, D., Providência, C., and Vidaña, I. (2013). Formation of hybrid stars from metastable hadronic stars. *Phys. Rev.* C88:055802. doi: 10.1103/PhysRevC.88.055802

Malik, T., Alam, N., Fortin, M., Providência, C., Agrawal, B. K., Jha, T. K., et al. (2018). Gw170817: constraining the nuclear matter equation of state from the neutron star tidal deformability. *Phys. Rev. C* 98:035804. doi: 10.1103/PhysRevC.98.035804

Maslov, K. A., Kolomeitsev, E. E., and Voskresensky, D. N. (2016). Relativistic mean-field models with scaled hadron masses and couplings:

hyperons and maximum neutron star mass. *Nucl. Phys.* A950, 64–109. doi: 10.1016/j.nuclphysa.2016.03.011

Masuda, K., Hatsuda, T., and Takatsuka, T. (2013). Hadron-quark crossover and massive hybrid stars with strangeness. *Astrophys. J.* 764:12. doi: 10.1088/0004-637X/764/1/12

Most, E. R., Weih, L. R., Rezzolla, L., and Schaffner-Bielich, J. (2018). New constraints on radii and tidal deformabilities of neutron stars from gw170817. *Phys. Rev. Lett.* 120:261103. doi: 10.1103/PhysRevLett.120.261103

Negreiros, R., Tolos, L., Centelles, M., Ramos, A., and Dexheimer, V. (2018). Cooling of small and massive hyperonic stars. *Astrophys. J.* 863:104. doi: 10.3847/1538-4357/aad049

Oertel, M., Hempel, M., Klähn, T., and Typel, S. (2017). Equations of state for supernovae and compact stars. *Rev. Mod. Phys.*, 89:015007. doi: 10.1103/RevModPhys.89.015007

Oyamatsu, K., and Iida, K. (2007). Symmetry energy at subnuclear densities and nuclei in neutron star crusts. *Phys. Rev. C* 75:015801. doi: 10.1103/PhysRevC.75.015801

Pais, H., and Providência, C. (2016). Vlasov formalism for extended relativistic mean field models: The crust-core transition and the stellar matter equation of state. *Phys. Rev.* C94:015808. doi: 10.1103/PhysRevC.94.015808

Pereira, R. C., Costa, P., and Providência, C. (2016). Two-solar-mass hybrid stars: a two model description with the Nambu-Jona-Lasinio quark model. *Phys. Rev.* D94:094001. doi: 10.1103/PhysRevD.94.094001

Potekhin, A. Y. (2014). Atmospheres and radiating surfaces of neutron stars. *Phys. Usp.* 57, 735–770. doi: 10.3367/UFNe.0184.201408a.0793

Potekhin, A. Y., Yakovlev, D. G., Chabrier, G., and Gnedin, O. Y. (2003). Thermal structure and cooling of superfluid neutron stars with accreted magnetized envelopes. *Astrophys. J.* 594, 404–418. doi: 10.1086/376900

Prakash, M., Prakash, M., Lattimer, J. M., and Pethick, C. J. (1992). Rapid cooling of neutron stars by hyperons and Delta isobars. *Astrophys. J.* 390:L77. doi: 10.1086/186376

Providencia, C., Avancini, S. S., Cavagnoli, R., Chiacchiera, S., Ducoin, C., Grill, F., et al. (2014). Imprint of the symmetry energy on the inner crust and strangeness content of neutron stars. *Eur. Phys. J.* A50:44. doi: 10.1140/epja/i2014-14044-7

Providencia, C., and Rabhi, A. (2013). Interplay between the symmetry energy and the strangeness content of neutron stars. *Phys. Rev.* C87:055801. doi: 10.1103/PhysRevC.87.055801

Raduta, A. R., Sedrakian, A., and Weber, F. (2017). Cooling of hypernuclear compact stars. *Mon. Not. R. Astron. Soc.* 475, 4347–4356. doi: 10.1093/mnras/stx3318

Raithel, C. A., Özel, F., and Psaltis, D. (2018). Tidal deformability from gw170817 as a direct probe of the neutron star radius. *Astrophys. J. Lett.* 857:L23. doi: 10.3847/2041-8213/aabcbf

Rüster, S. B., Hempel, M., and Schaffner-Bielich, J. (2006). Outer crust of nonaccreting cold neutron stars. *Phys. Rev. C* 73:035804. doi: 10.1103/PhysRevC.73.035804

Schaffner, J., and Mishustin, I. N. (1996). Hyperon-rich matter in neutron stars. *Phys. Rev. C* 53, 1416–1429. doi: 10.1103/PhysRevC.53.1416

Shen, H., Yang, F., and Toki, H. (2006). Double-Lambda hypernuclei in the relativistic mean-field theory. *Prog. Theor. Phys.* 115, 325–335. doi: 10.1143/PTP.115.325

Steiner, A. W., Lattimer, J. M., and Brown, E. F. (2016). Neutron star radii, universal relations, and the role of prior distributions. *Eur. Phys. J.* A52:18. doi: 10.1140/epja/i2016-16018-1

Steiner, A. W., Prakash, M., Lattimer, J. M., and Ellis, P. J. (2005). Isospin asymmetry in nuclei and neutron stars. *Phys. Rept.* 411, 325–375. doi: 10.1016/j.physrep.2005.02.004

Sugahara, Y., and Toki, H. (1994). Relativistic mean field theory for unstable nuclei with nonlinear sigma and omega terms. *Nucl. Phys.* A579, 557–572. doi: 10.1016/0375-9474(94)90923-7

Sugimura, H., Agnello, M., Ahn, J.K., Ajimura, S., Akazawa, Y., Amano, N., et al. (2014). Search for $^{6}_{\Lambda}$H hypernucleus by the ^{6}Li(π^{-}, K^{+}) reaction at $p_{\pi^{-}} = 1.2$ GeV/c. *Phys. Lett.* B729, 39–44. doi: 10.1016/j.physletb.2013.12.062

Tews, I., Margueron, J., and Reddy, S. (2018). Critical examination of constraints on the equation of state of dense matter obtained from GW170817. *Phys. Rev.* C98:045804. doi: 10.1103/PhysRevC.98.045804

Tolos, L., Centelles, M., and Ramos, A. (2017). The equation of state for the nucleonic and hyperonic core of neutron stars. *Publ. Astron. Soc. Austral.* 34:e065. doi: 10.1017/pasa.2017.60

Tsang, M. B., Stone, J. R., Camera, F., Danielewicz, P., Gandolfi, S., Hebeler, K., et al. (2012). Constraints on the symmetry energy and neutron skins from experiments and theory. *Phys. Rev.* C86:015803. doi: 10.1103/PhysRevC.86.015803

Tsang, M. B., Zhang, Y., Danielewicz, P., Famiano, M., Li, Z., Lynch, W. G., and Steiner, A. W. (2009). Constraints on the density dependence of the symmetry energy. *Phys. Rev. Lett.* 102:122701. doi: 10.1103/PhysRevLett.102.122701

Typel, S., Röpke, G., Klähn, T., Blaschke, D., and Wolter, H. (2010). Composition and thermodynamics of nuclear matter with light clusters. *Phys.Rev.* C81:015803. doi: 10.1103/PhysRevC.81.015803

van Dalen, E. N. E., Colucci, G., and Sedrakian, A. (2014). Constraining hypernuclear density functional with Λ-hypernuclei and compact stars. *Phys. Lett. B* 734, 383–387. doi: 10.1016/j.physletb.2014.06.002

Vidana, I., Logoteta, D., Providencia, C., Polls, A., and Bombaci, I. (2011). Estimation of the effect of hyperonic three-body forces on the maximum mass of neutron stars. *EPL* 94:11002. doi: 10.1209/0295-5075/94/11002

Vidana, I., Providencia, C., Polls, A., and Rios, A. (2009). Density dependence of the nuclear symmetry energy: a Microscopic perspective. *Phys. Rev.* C80:045806. doi: 10.1103/PhysRevC.80.045806

Warda, M., Viñas, X., Roca-Maza, X., and Centelles, M. (2009). Neutron skin thickness in the droplet model with surface width dependence: Indications of softness of the nuclear symmetry energy. *Phys. Rev. C* 80:024316. doi: 10.1103/PhysRevC.80.024316

Weissenborn, S., Chatterjee, D., and Schaffner-Bielich, J. (2012). Hyperons and massive neutron stars: vector repulsion and SU(3) symmetry. *Phys. Rev.* C85:065802. doi: 10.1103/PhysRevC.85.065802

Weissenborn, S., Chatterjee, D., and Schaffner-Bielich, J. (2013). Hyperons and massive neutron stars: vector repulsion and strangeness. *Nucl. Phys.* A914, 421–426. doi: 10.1016/j.nuclphysa.2013.04.003

Weissenborn, S., Sagert, I., Pagliara, G., Hempel, M., and Schaffner-Bielich, J. (2011). Quark matter in massive compact stars. *Astrophys. J. Lett.* 740:L14. doi: 10.1088/2041-8205/740/1/L14

Yakovlev, D. G., Levenfish, K. P., Potekhin, A. Y., Gnedin, O. Y., and Chabrier, G. (2004). Thermal states of coldest and hottest neutron stars in soft x-ray transients. *Astron. Astrophys.* 417, 169–179. doi: 10.1051/0004-6361:20034101

Yakovlev, D. G., and Pethick, C. J. (2004). Neutron star cooling. *Annu. Rev. Astron. Astrophys.* 42, 169–210. doi: 10.1146/annurev.astro.42.053102.134013

Zdunik, J. L., Fortin, M., and Haensel, P. (2017). Neutron star properties and the equation of state for the core. *Astron. Astrophys.* 599:A119. doi: 10.1051/0004-6361/201629975

Zdunik, J. L., and Haensel, P. (2013). Maximum mass of neutron stars and strange neutron-star cores. *Astron. Astrophys.* 551:A61. doi: 10.1051/0004-6361/201220697